UNIVERSITY OF CALIFORNIA SAN DIEGO

Evaporation from Air-Water Interfaces at Very Low Grashof Numbers

A dissertation submitted in partial satisfaction of the
requirements for the degree
Doctor of Philosophy

in

Engineering Sciences (Mechanical Engineering)

by

Jessica P. T. Medrado

Committee in charge:

Professor Carlos F. M. Coimbra, Chair
Professor Renkun Chen
Professor Jan Kleissl
Professor Ping Liu
Professor David Saintillan

2021

The dissertation of Jessica P. T. Medrado is approved, and it is acceptable in quality and form for publication on microfilm and electronically.

University of California San Diego

2021

DEDICATION

I dedicate my dissertation to my mother, Maria Helena, my father, Julio, and my two sisters, Kauara and Julia. Together they inspire me to pursue my dreams, to be honest with my feelings, to respect the feelings of those around me, to be free and give freedom and, most of all, to push my boundaries further whenever possible. They inspire me to love.

EPIGRAPH

An unexamined life is not worth living.

— Socrates

TABLE OF CONTENTS

LIST OF FIGURES

LIST OF TABLES

ACKNOWLEDGEMENTS

I would like to thank Prof. Carlos Coimbra, my doctoral advisor, who saw in me a potential for a scientific career that I was not aware of.

I would also like to thank Rich H. Inman, my former labmate, for all the patience and support I had when I first started the experimental part of this work.

I wish to thank Prof. Yousef Bahadori, my Professor and friend, for the immeasurable support during my final year as a Ph.D. student.

My sincerely thank to the entire University of California San Diego for being home during my Ph.D. years. A special thanks to the staff of the Geisel Library and to the building itself, where I spent countless hours deciphering complex details of my doctoral work.

Finally, I want to thank Alex Friedman for the immense love and care since day one, which undoubtedly made all the difference for me to arrive at the end.

Chapter 2, in full, is a reprint of the material as it appears in Pool Evaporation Under Low Grashof Number Downward Convection 2021. Medrado, J. P. T.; Inman, R. H.; Coimbra, C. F. M., International Journal of Heat and Mass Transfer, 181, 2021. The dissertation author was the primary investigator and author of this paper.

Chapter 3, in full, has been submitted for publication of the material as it may appear in Isothermal and Near-Isothermal Free Evaporation from Open Tubes. Medrado, J. P. T.; Inman, R. H.; Coimbra, C. F. M., International Journal of Heat and Mass Transfer, 2021. The dissertation author was the primary investigator and author of this paper.

Chapter 4, in full, is currently being prepared for submission for publication of the material. Medrado, J. P. T.; Inman, R. H.; Coimbra, C. F. M. The dissertation author was the primary investigator and author of this paper.

VITA

2016	B. S. in Mechanical Engineering *cum laude*, Universidade Federal de Minas Gerais, Brazil
2016-2021	Graduate Research Student, University of California San Diego
2021	Ph. D. in Engineering Sciences (Mechanical Engineering), University of California San Diego

PUBLICATIONS

J. P. T. Medrado, R. H. Inman, C. F. M. Coimbra "Pool Evaporation Under Low Grashof Number Downward Convection", *International Journal of Heat and Mass Transfer*, 181, 2021.

J. P. T. Medrado, R. H. Inman, C. F. M. Coimbra, "Isothermal and Near-Isothermal Free Evaporation from Open Tubes", *International Journal of Heat and Mass Transfer*, under review.

J. P. T. Medrado, R. H. Inman, C. F. M. Coimbra, "Non-Isothermal Free Evaporation from Open Tubes", in preparation.

ABSTRACT OF THE DISSERTATION

Evaporation from Air-Water Interfaces at Very Low Grashof Numbers

by

Jessica P. T. Medrado

Doctor of Philosophy in Engineering Sciences (Mechanical Engineering)

University of California San Diego, 2021

Professor Carlos F. M. Coimbra, Chair

The physics of air-water interface transport processes under very low mixing conditions is still poorly characterized due to the difficulty in balancing the combined heat and mass transfer mechanisms at play. Such processes are ubiquitous in lab facilities, biological systems and in a vast number of engineering applications. Correlations for mass transfer rates at very low Grashof numbers in weakly convective flows are not readily available, which often leads to incorrect estimations of evaporation rates derived from simplified 1-D models. This work investigates a number of fundamental free water-evaporation processes at very low Grashof (Gr) numbers.

First, the free evaporation from a small-scale circular pool at Gr numbers under dominant downward flow is examined. Experiments performed at normal conditions of temperature and

pressure (NCTP) and for a wide range of relative humidity values are described and compared to numerical simulations. A downward thermally-induced flow originated at the rim of the pool overcomes the concentration-induced buoyancy, consequently forcing the far-stream dry air to descend into the lower temperature air-water interface. Experimental results show that a somewhat stable steady-state recirculation zone near the air-water interface develops for Gr numbers greater than or equal to 50. The Sherwood number (Sh) for this geometry scales with $Gr^{1/4}$ for drier free-stream boundary conditions, while it approaches a constant value for smaller mass transfer potentials (i.e., wetter environments). A Sh number correlation as a function of Gr number is proposed, covering Gr numbers from 10 to 10^5.

The mass transport dynamics is also analysed for free evaporation from open tubes. The mass transport results in complex patterns due to the interaction between the vertical walls and the buoyant flow. Evaporation undergoes a multi-regime process where, depending on the driving potential, stable convective cells develop inside the tube. These convective cells enhance the evaporation rate in most circumstances. The dependence of the diffusion-driven and convection-driven regimes as functions of the geometrical aspect ratio of the tube is studied. A new Sh number correlation valid for Gr numbers ranging from 50 to 4,000 is proposed. This correlation, which is nearly invariant with temperature, expresses the relationship between the Sh and Gr numbers for varying aspect ratios.

Chapter 1

Introduction

Evaporation of water has been studied in detail for decades. Most of the published work concerns with forced evaporation, where usually forced convection (i.e., a heated body of liquid or forced gas stream) is used to impart high mass transfer rates at the gas-liquid interface [9, 11, 48, 20, 21, 49]. On the other hand, evaporation process without forced convection into the system has been investigated less often due to the sensitivity of the flow to boundary conditions. There is a clear need to investigate unforced convection transport processes in order to avoid usage of inappropriate mass transfer rate correlations in practical applications.

Free evaporation (under unheated conditions) occurs due to a difference in water vapor concentration at the two sides of the interface. Mass concentration gradients under gravitational body forces in turn induce convective motion. Because inertial, gravitational and viscous forces are all generally weak under free conditions, usually negligible radiation effects also become important. As a result, consideration of non-linear first order and higher order terms in the governing equations and boundary conditions require simultaneous solution. Despite the fact that evaporation can develop under (quasi) isothermal conditions, in most free convection cases interface cooling will develop and induce a measurable temperature drop at the gas-liquid interface. The temperature drop increases with the mass driving potential, and in general results in gas-side

temperature gradients that are in opposite direction with respect to the mass concentration gradients. For horizontal gas-liquid interfaces with non-unity Lewis numbers, this opposing transport mechanism results in complex patterned recirculation zones even at very low Grashof (Gr) numbers.

As discussed by Sharpley, Boelter, Gordon, and Griffin [39, 6], small water vapor concentration differences results in substantial changes in the flow structure above the air-water interface of a small pool. When the concentration difference is relatively high (e.g., heat supply at the liquid side) the flow is directed primarily upward (also referred to as parallel-flow evaporation), a rising plume will form above the interface with the saturated air leaving in an upward jet structure. As the concentration difference decreases (approaching the limit of free evaporation), the mixture above the air-water interface is denser, leading to a dominant downward flow, which is also know as contraflow. To interpret these two distinct flow configurations, a common approach is to assume that a boundary layer forms at the interface, while the temperature of the liquid remains fixed at some predefined value [50]. The dry air enters the boundary layer from the edges of the container when the temperature of the water is higher than the ambient temperature. In this case, the incoming air is characterized by a quasi-stagnant velocity and enters the boundary layer at near ambient temperatures. If instead, the surface water is colder (but not so cold as to induce condensation), the dry air will enter the boundary layer at the center of the interface.

Several studies on water evaporation from a heated liquid pool have been conducted. Sharpley and Boelter [39], provided some of the earliest results suggesting a correlation of the form $Sh = C\,Sc^{1/3}Ra^{n}$, where C is constant, to estimate the evaporation rate from heated pans in quiescent air. These earlier correlations were based solely on experimental observations. Similar studies were later conducted by Boelter et al. [6], Sparrow et al. [42] and more recently by Bower and Saylor [9]. Bower and Saylor [9, 10] concluded that for an upward convection, the power n is affected by turbulence and restrictions of the flow in the proximity of the air-water interface. For example, power n values found from experimental investigations ranged from 0.213

to 0.306. Dollet and Boulogne [17] also studied evaporation under upward convection, but for an isothermally evaporating disk, with the disk geometry defined as a circular evaporating surface laying on an infinite plane. In their work, the authors derive a Sh number correlation based on the flux from different zones that theoretically develop in the boundary layer above the air-water interface. They suggest a correlation where $Sh_R \sim \pi/2\,(C_1 + C_2\ Gr_R^{1/5})$ with constants C_1 and C_2 obtained from experimental results. Among the Sh number correlations, Sparrow et al. [42] is the most relevant for evaporation driven by downward flow, a flow structure present in processes where the air-water interface is colder than the surrounding. The low-temperature interface results in opposing thermal-concentration buoyant effects.

The boundary layer approach is generally not valid when small scale pool evaporation processes occur in the presence of opposing thermal-concentration buoyant flows due to inexistence of a length scale that is much smaller than the integral length scale. Opposing thermal-concentration effects may induce the formation of recirculation zones, which render the analysis of the flow by analytical methods more challenging. In buoyant flows originating from a flat horizontal surface, the direction of buoyancy is often orthogonal to the horizontal surface, and for fluids charecterized by $Sc \neq Pr$ ($Le \neq 1$) the boundary layer approximation is not applicable due to development of stagnation regions with associated recirculation zones near the surface [37, 44]. These stable but weak flow fields create additional challenges for experimental observation at such low Gr number flows, ultimately limiting the range of available correlations.

When it comes to the evaporation from open tubes, the 1-D stagnant film solution — often referred to as the "Stefan diffusion tube" or "Stefan tube" solution, is the most common approach. The Stefan tube solution allows for high mass transfer (convective) rates at the interface, but it is essentially a diffusion-controlled process where only one species (the vapor at the interface) is transported while the background species (air) is stationary. Particularly with respect to aqueous solutions, high mass transfer rates that require convective corrections are never experienced under Normal Conditions of Temperature and Pressure (NCTP). Conditions required for the 1-D

solution, in fact, are very often not satisfied in practice. The required conditions mainly depend on tubes with a large aspect ratio (slender tubes, sometimes referred to as small diameter tubes or long tubes) [23, 29, 21, 49], processes occurring in a relatively wet environment while a sweeping air stream is imposed over the open-end to establish a locally predefined concentration. Reducing the evaporation from an open tube to a 1-D problem when these conditions are absent can be highly inaccurate.

Buoyancy effects driven by the difference of molecular weights between air and water causes an air-side convective mixing that substantially affects evaporation rates when compared to 1-D model solutions of open tube evaporation. Even in the simplified 2-D Stefan diffusion tube (axisymetric), the introduction of buoyant effects added to the interaction of the flow with vertical walls lead to a rather complex velocity and mass concentration profiles [33, 29]. Convection due to buoyancy inside tubes can manifest according to different modes, with the first mode being the diametrically-antisymmetric (asymmetric) flow, in which only one convection cell is observed inside the tube [47, 22, 36, 13].

Free evaporation from open tubes (i.e., no imposed conditions such as solvent stream at the open-end) was first investigated by Nunez and Sparrow [35], where the authors studied how the buoyancy would impact the Stefan tube solution. To account for natural convection, they imposed axial symmetry to solve the conservation equations in the radial and vertical coordinates. Axial symmetry was subsequently adopted by Sparrow and Nunez [43] and Hsieh and Kuo [24]. Finally, through a detailed numerical and experimental investigation of open tube evaporation, McBain et al. [30] suggested that the fluid flow inside the tube is not axially symmetric in all situations, but instead experience the diametrically antisymmetric configuration. In this case, flow from the surrounding would enter the open tube from one of its sides and leave through the opposite side. To numerically simulate this condition, they first used a slightly tilted gravitational field to establish the diametrically anti-symmetric mode of the flow. The result was then used as a first guess solution to the subsequent non-tilted steady-state simulation. After running the

free evaporation of water for a range of Gr numbers, they were able to accurately predict the dimensionless evaporation rate, the Sh number, for an aspect ratio (AR) equal to 4 (AR being the ratio between the distance from the air-water interface to the open-end and the radius of the tube, L/R), with agreement between theory and experiments. The diametrically anti-symmetric model allowed them to correct at which critical Gr number the onset of the convection driven regime would occur: a value 5 times lower than what was estimated from axially symmetric models [30]. It is worth mentioning that Zion et al. [25] also studied the evaporation from different geometries including open tubes (referred to by the authors as well), however for the evaporation of a heavy solute (hydrocarbons) in a light solvent (air). They concluded that for this specific condition, buoyancy has a negligible effect on the evaporation rate from an open tube (well), resulting in the process being diffusion-dominated and therefore the 1-D approximation sufficient to estimate the evaporation rate.

For a light solute evaporating in a heavy solvent (i.e., water into air), McBain et al. [30] demonstrated that blowing effects are negligible at the gas-liquid interface for processes at low Gr numbers. Instead, the strong buoyancy is what brings the evaporation problem into regimes mostly dependent on the multidimensional distribution of the species concentration at the air-side. Yet, despite their important contribution, numerous questions regarding free evaporation from open tubes remain unanswered and because of that, existing mass transfer correlations are not available in the literature.

In order to cover the gap related to free evaporation, this work investigates two distinct evaporation systems: free evaporation from pools and from open tubes. While the former represents the case of unbounded natural convection driven by free evaporation, in the later constraint domain effects are introduced as buoyancy is bounded by the walls of the container. Both systems are numerically and experimentally investigated across a wide range of background relative humidity values under NCTP. Experimental results are obtained from a pressure-temperature-humidity controlled chamber which defines the far stream conditions for the boundary-value problem. A

high precision balance placed inside the chamber measures the amount of liquid evaporating for the ascribed conditions of temperature, pressure and relative humidity. Temperature sensors and a hygrometer measure the respective temperature and relative humidity far away from the evaporating surface during the process. A finite-element numerical model is applied to the same experimental conditions. In the model, the mass, momentum and energy conservation equations are simultaneously solved for the given far-stream or environmental (in this work also referred to as the e-state) conditions. Because the evaporative processes under study here are weak, quasi-steady laminar flow conditions are assumed for each e-state. Moreover, boundary conditions at the interface are in accordance with the balance between heat diffusive-convective and mass flows from the liquid side, from the gas side and from surface radiation, as all contribute to the heat of vaporization due to the ongoing phase change process. The agreement between numerical and experimental results allows for the extending of numerical simulations to a vast range of geometrical aspect ratios and thermodynamic states. Based on the validated numerical results, Sh number correlations as functions of the Gr numbers are then proposed for pool evaporation and open tube evaporation.

Chapter 2

Pool evaporation

Natural convection driven by free evaporation of water into moist air is a complex multi-physics process involving combined heat and mass transfer. The Grashof numbers (Gr) relevant to laboratory-scale evaporation of water in air under gravitational forcing range from unity to several million. While several studies was conducted to characterize high Gr number flows, small Gr number processes lack examination since they are prone to the intermittent formation of toroidal ring-like jets and recirculation zones near the air-water interface. Nonetheless, detailed rates of water evaporation into air under low Gr numbers are needed to understand a number of natural processes and engineered applications such as spore dispersal mechanisms developed by fungi [18], water desalination systems [2], geothermal engineering [8, 7] and microscopic DNA mapping [3, 19]. Several recent papers investigate geometrical, composition, and surface related effects on gravitationally-driven liquid evaporation under different environmental conditions (see, e.g., [12, 26, 48, 11, 14]).

Here, we study Gr number regimes relevant to the common phenomena involving pool sizes comparable to a glass of water or a laboratory beaker, where opposig bouyant effect and recirculation zones above a horizontal air-water interface are present. We develop precision-controlled experiments and appropriate numerical simulations to study stable conditions that

naturally form from the thermally-driven downward convection towards the interface. For Gr numbers on the order of 50 and above, experimental results reveal that the recirculation zone is stable, that is, moderate heterogeneities of the surrounding impart a negligible effect in the net mass and heat transfer.

In addition to carefully designed experiments, we use Finite Element Model (FEM) numerical simulations to simulate the natural convection due to evaporative processes in the presence of downward thermal and upward concentration buoyancy induced flows. The simulations are carried on without the need to enforce a predefined temperature at the interface, thus reproducing the experimental setup. As such, we allow evaporative cooling to take place so that there is equilibrium at the air-water interface for given environmental temperatures and relative humidities. Boundary conditions at the interface are defined in accordance to heat and mass balances such that the heat of vaporization is the sum of the diffusive-convective heat flow contributions from the liquid side, from the gas side and from surface radiation. Because mass fractions of water vapor in air are small at room temperatures (low mass transfer process), the downward thermal-induced buoyant force dominates over the concentration-induced buoyancy, which results in a net downward oriented flow in the far-stream field, sustained by a toroidal ring-like jet originating at the rim of the pool. Numerical simulations then extended to lower Gr numbers indicate that the Sh number converges to a nominal value (the pure diffusion limit). In the light of this result, we propose a universal correlation valid for a range of Gr numbers between 10 and 100,000.

2.1 The physical problem

Water evaporates from a cylindrical container in a controlled environment. Constant values of temperature, pressure and relative humidity away from the air-water interface define both the thermodynamic condition and the water vapor concentration of the (far-stream) environment, or the e-state (see Figure 2.1). Under quasi-steady conditions, the evaporation process achieves a

near-stationary rate for each combination of T_e, P_e and RH_e. Gravity-induced natural convection due to thermal and concentration gradients are the main driving mechanisms for fluid motion on the gas side. For modeling purposes, we assume the buoyant forces to follow the Boussinesq approximation, where the density variations are considered to be relevant only in the buoyancy terms of the momentum equation. The radius of the container is the length scale of interest for both the thermal and mass Grashof numbers:

$$Gr_{R_T} = \frac{g\beta_T(T_s - T_e)R^3}{\nu_g^2} \tag{2.1a}$$

$$Gr_{R_m} = \frac{g\beta_m(m_{1,s} - m_{1,e})R^3}{\nu_g^2} \tag{2.1b}$$

as well as for the Sherwood number:

$$Sh_R = \frac{\mathscr{J}_{m_1} R}{\rho \mathscr{D}_{12}} = \frac{\dot{m}'' R}{\mathscr{B}_{m_1} \rho \mathscr{D}_{12}} \,. \tag{2.2}$$

The interface mass flux $\dot{m}''$ and the mass driving potential $\mathscr{B}_{m_1}$ are related through the mass transfer conductance of species 1 (water vapor) $\mathscr{g}_{m1}$ as $\dot{m}'' = \mathscr{g}_{m1}\mathscr{B}_{m_1}$, while the mass driving potential is defined as (for more details see reference [34])

$$\mathscr{B}_{m_1} = \frac{m_{1,s} - m_{1,e}}{1 - m_{1,s}}. \tag{2.3}$$

The average Sherwood number is expressed as a function of the combined thermal and concentration Grashof number, and averaged over the entire surface area of the air-water interface s.

The heat flux from the liquid side, from the gas side, and the radiative heat exchange between the air-water interface and the surrounding environment all play a part in determining the combined heat and mass transfer rates for given conditions. The sensible, latent and radiative heat

fluxes are all very small in this problem, so the relative balance between each of these different transfer mechanisms requires careful consideration. Here we assume an infinitely thin interface without impurities, which leads to temperature continuity (i.e., thermal equilibrium) on both sides of the air-water interface. The interface temperature drops due to the loss of thermal energy from the liquid molecules left in the liquid state as water molecules evaporate into the vapor phase. Due to the high enthalpy of vaporization of water, the temperature drop at the interface is felt throughout the depth of the liquid pool. The liquid pool is shallow for its characteristic conduction length scale, therefore convection and surface tension circulations induced by small thermal and density gradients on the liquid side are weak, so that the heat flux from the liquid side to the interface approaches the value found by considering a hydrostatic pool with no circulation induced by thermal effects. However, the nonslip condition at the air-water interface induces liquid motion, and this effect is taken into account in our numerical simulations. Under normal conditions of temperature and pressure, the equilibrium saturation temperature (approximately the wet bulb temperature) and associated mass fraction of water vapor on the gas side are both too small to induce Stefan flow across the interface, so the problem under study here involves low mass transfer rates only.

Overall, the low mass transfer rate process is a combined heat and mass transfer problem regulated by a delicate balance between natural convection and radiative heat transfer rates. The convective transfer process results from complex gravity-induced flow patterns on the gas side of the interface.

2.1.1 Governing equations and boundary conditions

On the liquid side, the governing equations for mass, momentum, and energy conservation are:

$$\nabla \cdot \mathbf{u} = 0 \,, \tag{2.4}$$

$$\mathbf{u} \cdot \nabla \mathbf{u} = -\frac{1}{\rho_l} \nabla p + \nu_l \nabla^2 \mathbf{u} \,, \tag{2.5}$$

$$\mathbf{u} \cdot \nabla T = \alpha_l \nabla^2 T \,. \tag{2.6}$$

The governing equations on the gas side are also derived from the mass, momentum, energy and species conservation equations. The gas is considered a binary ideal gas system formed by water vapor and dry air:

$$\nabla \cdot \mathbf{u} = 0 \,, \tag{2.7}$$

$$\mathbf{u} \cdot \nabla \mathbf{u} = -\frac{1}{\rho_g} \nabla P + \nu_g \nabla^2 \mathbf{u} + g \, (\beta_m \Delta m_1 + \beta_T \Delta T) \, \hat{\mathbf{k}} \,, \tag{2.8}$$

$$\mathbf{u} \cdot \nabla T = \alpha_g \nabla^2 T \,, \tag{2.9}$$

$$\mathbf{u} \cdot \nabla m_1 = \mathscr{D}_{12} \nabla^2 m_1 \,. \tag{2.10}$$

The symbol P indicates pressure (including the gravitational potential $p + gz\rho_g$), and the symbols β_m and β_T are respectively the mass and thermal volumetric coefficients of expansion. More details about these coefficients are given in Appendix A. Since the absorption of air in water is negligible, we assume that only one species is being transferred (water vapor and denoted by the subscript 1) at the interface.

The set of governing equations are subjected to the following boundary conditions (see

Figure 2.1.a for reference). At all surfaces at the e-state we have

$$\mathbf{u} = 0 \,, \tag{2.11a}$$

$$T = T_e \,, \tag{2.11b}$$

$$m_1 = m_1\left(\mathrm{RH}_e,\, T_e\right) \,, \tag{2.11c}$$

$\forall\, x, y, z$ in e.

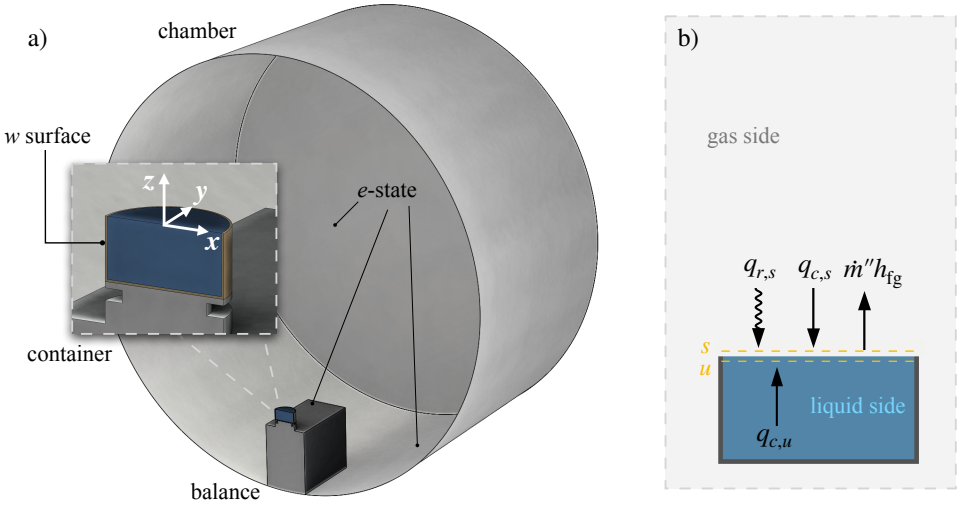

Figure 2.1: a) Schematic view of the experimental setup and the coordinate system of reference used in the study of water evaporating from a small container. The origin of the coordinate system is at the air-water interface. At the e-state, values of the temperature, pressure and mass concentration of water vapor are known (determined by measurements). b) Schematic of the energy transport dynamics at the air-water interface. The interface receives energy from radiation $q_{r,s}$, gas-side convection $q_{c,s}$ and liquid-side convection $q_{c,u}$, while releasing thermal energy through $\dot{m}'' h_{\mathrm{fg}}$ as the water evaporates.

At the air-water interface (using the Cartesian coordinate system depicted in Fig. 2.1):

$$u_x\ (z=0^+) =\ u_x\ (z=0^-)\ , \tag{2.12a}$$

$$u_y\ (z=0^+) =\ u_y\ (z=0^-)\ , \tag{2.12b}$$

$$u_z = 0\ , \tag{2.12c}$$

$$\mu_g \frac{\partial u_x}{\partial z}\bigg|_{z=0^+} =\ \mu_l \frac{\partial u_x}{\partial z}\bigg|_{z=0^-}\ , \tag{2.12d}$$

$$\mu_g \frac{\partial u_y}{\partial z}\bigg|_{z=0^+} =\ \mu_l \frac{\partial u_y}{\partial z}\bigg|_{z=0^-}\ , \tag{2.12e}$$

$$T(z=0^+) =\ T(z=0^-) = T_s(r)\ , \tag{2.12f}$$

$$-\rho_g \mathscr{D}_{12} \frac{\partial m_1}{\partial z}\bigg|_{z=0^+} h_{\mathrm{fg}} + \varepsilon\sigma(T_s^4 - T_e{}^4) = -k_g \frac{\partial T}{\partial z}\bigg|_{z=0^+} - k_l \frac{\partial T}{\partial z}\bigg|_{z=0^-}\ , \tag{2.12g}$$

$$m_1\ =\ m_1\,(P_{\mathrm{sat}},\ T_s)\ , \tag{2.12h}$$

$\forall\ x, y$ in s, and for z also in s ($z = 0$). The symbol $\mathscr{D}_{12}$ refers to the binary diffusion coefficient of water vapor in air [34] (see appendix), h_{fg} to the enthalpy of vaporization evaluated at T_e, and ε to the emissivity of the water, here considered as a blackbody for longwave radiation. Note that the interface energy balance (Eq. 12g) implies low mass transfer rates explicitly, as expected for a air-water interface at ambient temperatures. Inclusion of Stefan fluxes does not change the numerical results for the conditions under study.

The water vapor at the interface is saturated at the local interface temperature, T_s. The mass fraction m_1 depends on the partial pressure of species 1, which in turn depends on the

saturation pressure. The saturation pressure for water vapor is obtained according to the Tetens equation of state [46], as described in the appendix.

Continuity of temperature and continuity of heat flow are imposed between the vertical walls of the container and the surrounding fluid (water or air), while zero mass flux is applied at the walls of the container exposed to the gas side:

$$T = T_{\mathrm{f}} \,, \tag{2.13a}$$

$$\mathbf{n} \cdot q = k_{\mathrm{f}} \nabla T|_{\mathrm{f}} \,, \tag{2.13b}$$

$$\nabla m_1 = 0 \,, \tag{2.13c}$$

$\forall\, x$ in $w, \forall\, y$ in w and $\forall\, z$ in w.

In order to investigate the effect of boundary conditions at the bottom of the liquid pool, we consider two different conditions: specified temperature equal to T_e (equivalent to assuming a thermal reservoir at temperature T_e under the container); and zero heat flow at the bottom of the pool. The real condition depends on the thermal losses by the pool walls. In this study, the dimensions of the pool were selected to minimize surface tension (meniscus) and internal circulation effects.

2.2 Mass transfer correlations

The Sherwood number Sh for forced flow evaporation can be expressed as $Sh = Sh_0 + CRe^m Sc^n$, so that

$$Sh = Sh_0 + C \left(\frac{U_c L_c}{\nu} \right)^m \left(\frac{\nu}{\mathscr{D}_{12}} \right)^n \,, \tag{2.14}$$

in which Sh_0 is the dimensionless mass transfer rate in the pure diffusion limit, U_c the characteristic velocity and L_c the characteristic length. The exponent m is 1/2 for laminar flow and approaches 4/5 turbulent flow, whereas the exponent n is 1/3 for Pr numbers higher than 0.5 in laminar flows.

In free evaporation, the characteristic velocity of the flow depends on the ambient condition into which the process is subjected. In a dry atmosphere, for instance, the velocity of the gas reaches values on the order of 10^{-2} m/s. Since in this problem the characteristic length is on the order of centimeters, the Grashof number is of order 10, indicating that the inertial forces are slightly dominant over the viscous forces. Under this circumstance, the buoyancy term in the conservation of momentum equation scales with the convective term, resulting in a characteristic velocity proportional to the square root of the total Grashof number:

$$O\left(\frac{U^2}{L}\right) \sim O(g\beta_T(T-T_e) + g\beta_m(m-m_{1,e})), \tag{2.15a}$$

or

$$U \sim \frac{\nu}{L_c} Gr_{L_c}^{1/2}. \tag{2.15b}$$

For evaporation occurring at high relative humidity, the velocity of the system tends to zero due to the weaker driving forces, in turn leading to a buoyant force proportional to the viscous forces and the characteristic velocity proportional to the total Grashof number:

$$O\left(\nu\frac{U}{L_c^2}\right) \sim O(g\beta_T(T-T_e) + g\beta_m(m-m_{1,e})), \tag{2.16a}$$

$$U \sim \frac{\nu}{L_c} Gr_{L_c}. \tag{2.16b}$$

The Sherwood number would then become proportional to $Gr^{1/2}$. However, the temperature and mass concentration gradients are greatly reduced in this condition, which lead to

variations in the Sherwood number likely negligible for Grashof numbers near zero. As a result, for Grashof numbers near zero the dimensionless evaporation rate would be around the diffusion limit value, that is

$$Sh = Sh_0 + C_a Sc^{1/3} Gr^{1/2} \approx Sh_0 \tag{2.17a}$$

to then increase proportionally to the 1/4 power on the Grashof, as the Grashof number increases:

$$Sh = C_b + C_c \, Sc^{1/3} Gr^{1/4}. \tag{2.17b}$$

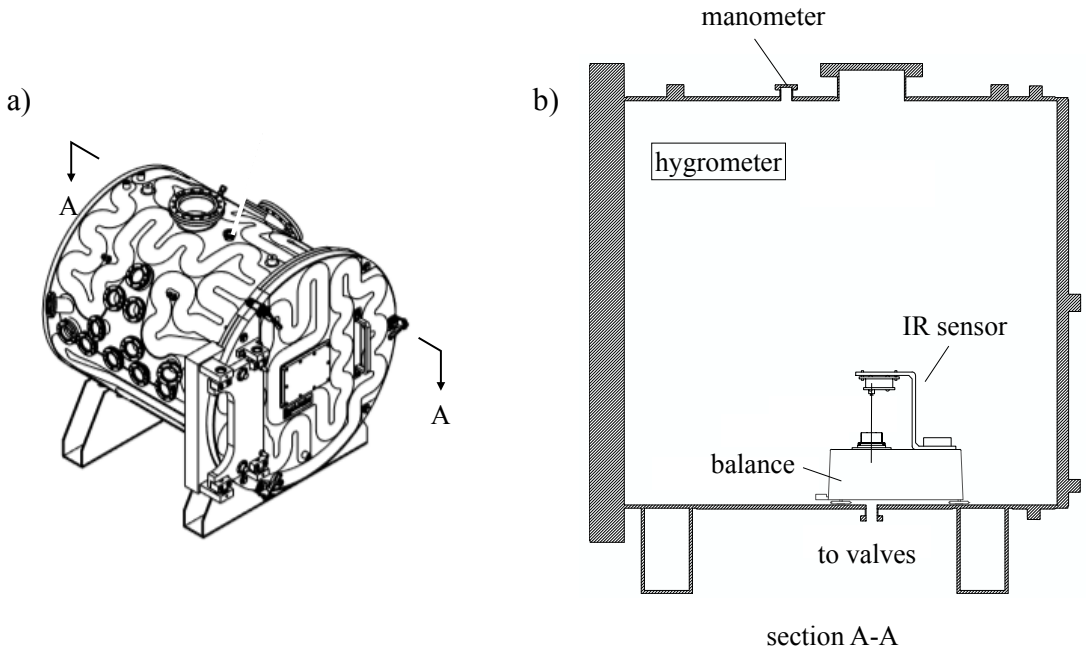

Figure 2.2: Schematic view of the vacuum-sealed chamber (a) and its interior (b, section A-A), the experimental setup used to measure the evaporation rate of water from a small container under downward convection. The high precision balance weights the remaining liquid water inside the pool as water evaporates. A hygrometer positioned away from the pool records the relative humidity inside the chamber. A manometer positioned on top of the setup reads the interior pressure, and 10 thermocouples type-K (not shown in the Figure) spread throughout read the chamber's interior and wall temperatures. A downward-facing infrared (IR) sensor measures the averaged air-water interface temperature.

2.3 Experimental method

A small container is completely filled with water and left to evaporate inside a vacuum-sealed chamber, as shown in Figure 2.1. The atmosphere of the chamber is thermodynamically controlled and the container is placed over a high precision balance (4212B-102, A&D) that measures the remaining amount of liquid water. The chamber, made of stainless steel 304L, has a cylindrical shape with the inner diameter and inner length respectively around 0.3 m and 0.7 m in size. The longitudinal axis of the chamber is in the horizontal position, with the balance placed in the center as showed by Figure 2.1. The chamber was manufactured to have channels along the walls serving as passages for a working fluid driven by a chiller (Thermo Scientific Accel 500 LT). Through the recirculation of the working fluid it is possible to set the temperature of the walls of the chamber to a desired value.

The chamber is properly equipped with sensors that allow the full control over its thermodynamic state. A high precision chilled mirror dewpoint hygrometer (Optidew Remote, Michell) is used to measure the relative humidity of the chamber's interior. The relative humidity is decreased by forcing the air against a compartment filled with molecular sieve, which retains the water vapor molecules in its pores while drying out the air. Ten type K thermocouples are used to measure the temperature inside the chamber, 6 of which are directly attached to the walls. The inside pressure can be set to any value within the range of 1 to 0.1 atm. Once defined, the pressure at which the experiment is conducted is kept constant while a capacitance manometer (CMX1, Brooks Instrument) records the pressure level. Lastly, the temperature of the air-water interface is measured by an infrared sensor (1045 B, Phidgets) with a 10° field of view. The sensor is positioned in such a way as to read only the average temperature associated with the interface. Figure 2.2 is a schematic depiction of the experimental setup.

For each experimental run, the balance is re-calibrated and the hygrometer reset. In order to assure that the system is in quasi-steady state, the first one to two hours after the preparation

stage are discarded. As the water evaporates, the level of water in the container decreases, and to guarantee that the container stays completely filled during the measurements, the entire process is repeated for different targets of relative humidity. No mechanism keeping the relative humidity constant is applied during the experiments, in an effort to avoid disturbances influencing the system and, as consequence, the relative humidity continuously increases as the experiment goes on. However, owed to the fact that natural evaporation is a slow process, the same experiment can still be considered in quasi-steady state if it is divided into sub-experiments with sufficiently small relative humidity variation. Here, the sub-experiment is a time window in which the difference between the maximum and minimum relative humidity values is less than 1%.

After the experimental run finishes, a series of mass fluxes are obtained by performing a linear regression on the acquired mass and time data belonging to the selected time window (or to the sub-experiment, as explained previously). A χ^2 test is used to determine the number of degrees of freedom (DOF - number of data points minus the number of parameters in the fit) to be used, in which the number of DOF is progressively increased until it includes all the values in the respective window, starting with a minimum of 200 DOF. The mass flux is obtained from the data range correspondent to a number DOF yielding the best goodness of fit. All the other measured variables are calculated as the average of all the values belonging to the selected range.

Table 2.1: Mesh independence study for the numerical simulation of water evaporating from a small pool, showing the average Sherwood number for different quantities of triangular elements at the interface and total degrees of freedom (DOF) in the mesh.

Total DOF	Triangles	$\overline{Sh}_R$	% diff.
59,136	106	2.801	-
108,602	230	2.739	2.2 %
205,723	475	2.704	1.3 %
394,483	976	2.692	0.4 %
778,147	1965	2.683	0.3 %

2.4 Numerical method

A three-dimensional geometry, composed by the gas and liquid domains is solved using COMSOL Multiphysics^{TM}, which employs the finite element method for the solution of boundary value problems. We implement the governing equations along with the boundary conditions in a steady-state simulation using a direct solver, and apply a relative residual tolerance of $10.^{-3}$ To account for the cooling effect due to the phase change of water, we consider the interface as a boundary heat source in which energy is lost through heat of vaporization and energy is added through radiative heat exchange. The sum of all heat fluxes is compared to the total heat of vaporization for every numerical simulation, as a means to check the fidelity of the energy balance (Eq. 2.12g). All differences found were smaller than 0.05%. The water container is modeled as a shell since the thickness of the water container is considerably smaller than the characteristic length of the chamber (<1 mm vs. 300 mm). We enforce continuity of temperature and continuity of heat flux between the walls and the surrounding fluid. In order to employ fluxes as boundary conditions, the method of Langrange multipliers was used instead of directly taking the local gradient of the variables in question.

The geometry is discretized using tetrahedral elements, including a thorough mesh refinement near the air-water interface. Results between nodes in the mesh are interpolated using cubic shape functions. A mesh independence study is reported in table 3.1, with the Sherwood number given in terms of the number of triangles at the interface as well as in terms of the total degrees of freedom. One can notice that using more than approximately 1000 triangle elements at the interface results in minor changes of the Sherwood number.

2.5 Results

Here we show the central result of this study, a Sh-correlation valid for Grashof numbers in a range of 10 to 10^5. The correlation is obtained from numerical results in excellent agreement

Table 2.2: Sherwood number values for the evaporation from a small pool in the purely diffusive limit as a function of the ratio H/R.

H/R	1/3	1	2	5	10
$\overline{Sh}_R$	2.4	2.1	2.0	1.9	1.9

with experimental data, covering a wide range of temperature and relative humidity conditions. Overall, the correlation recovers the pure diffusion limit as the Grashof number goes to zero and obeys the scaling law followed by unbounded free evaporation.

2.5.1 Evaporation in the purely diffusive limit

In the purely diffusive limit, the velocity of the system is zero and both the temperature and the species concentration fields satisfy the Laplace equation. Boundary conditions are given by equations 2.11, 2.12 (with all velocities equal to zero) and 2.13. The problem of free evaporation from a pool at the purely diffusive limit is analogous to the electrostatic problem of two oppositely charged circular parallel conducting disks of radius a separated by a distance ka. The potential

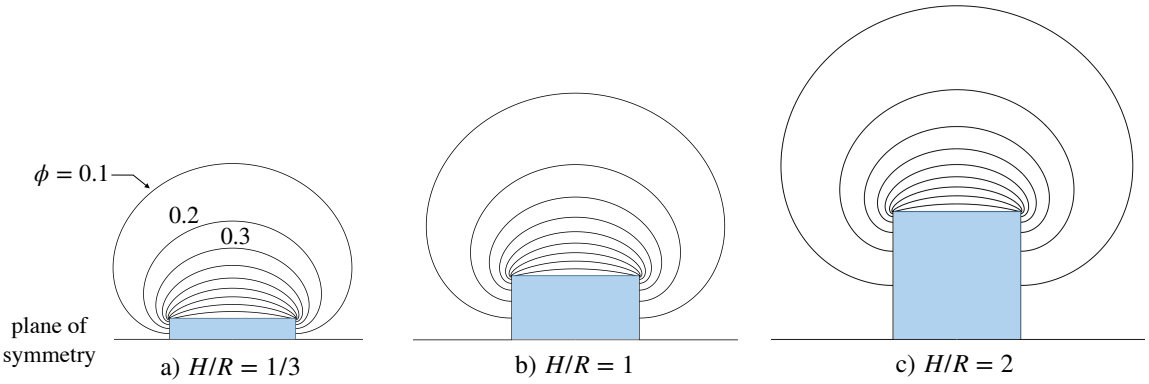

Figure 2.3: Normalized water vapor mass concentration ϕ for water evaporating into air from a small pool in the pure diffusion limit. The results are obtained from numerical simulations, according to three different H/R ratios. The water vapor mass concentration isosurfaces approach asymmetric oblate spheroidal shapes. When the container is short, the concentration isosurfaces near the container's walls are confined to a small region, yielding maximum evaporation rates. The isosurfaces spread apart as the container height is increased, until a point after which increasing the container's height has no significant effect on evaporation rates. See table 2.2 for complementary information.

field in this case is made of plane-symmetric spheroids superposing each other [28, 4]. In the case of free evaporation from a pool with no convection, numerical results also indicate that the water vapor concentration profiles are plane-symmetric spheroids (see Figure 2.3) with the plane of symmetry defined by the plane supporting the pool. Far away from the air-water interface, the water vapor concentration remains at a predefined value according to the far-stream relative humidity condition. The evaporation rate depends weakly on how far the air-water interface is from the plane of symmetry, that is, the height of the pool - an analogous interpretation to the charged disks problem where decreasing the separation between plates increases the influence of charge distribution from one plate to the other [4].

One difference between the evaporation from a pool under negligible convection and the oppositely charged parallel disks is that, in the former, there is a zero flux boundary condition at the walls of the container, while in the latter such condition is nonexistent. Figure 2.3 shows the normalized mass concentration ϕ for three different heights, while table 2.2 contains the respective Sherwood number values. In short containers, the distribution of the isolines of mass concentration near the walls is confined into a small space, forcing slightly higher mass fluxes. As the height of the pool increases, the isolines of water vapor become gradually less compressed, until a point in which increasing further the height produces no significant effect.

Under the idealized scenario of a purely diffusive regime, the Sh number shows a weak dependency on the height of the pool, as demonstrated by the results of numerical simulations in the pure diffusion limit (table 2.2). Since such dependence is weak, it is reasonable to expect that the Sh number (based on the radius of the pool) asymptotes to values around 2 when the Gr number approaches zero for a wide range of pool heights.

2.5.2 Evaporation under downward flow motion

Figure 2.4 shows the mass flux along with the temperature of the interface as a function of relative humidity for different ambient conditions, and for the container having either a fixed temperature at the bottom (290 K and 310 K test), or zero-flux (300 K test). As one can see, the numerical results closely describe the experimental data in all cases. The good agreement between theory and experiment corroborates the use of the simplified boundary conditions used in the numerical simulations for the far-stream. There is in fact a considerable temperature drop at the interface caused by evaporative cooling that creates thermal gradients on both the liquid and gas side. It is also important to recognize that this drop in interface temperature is strongly dependent on the evaporation rate.

In an isothermal system there exists only positive buoyancy generating an upward flow

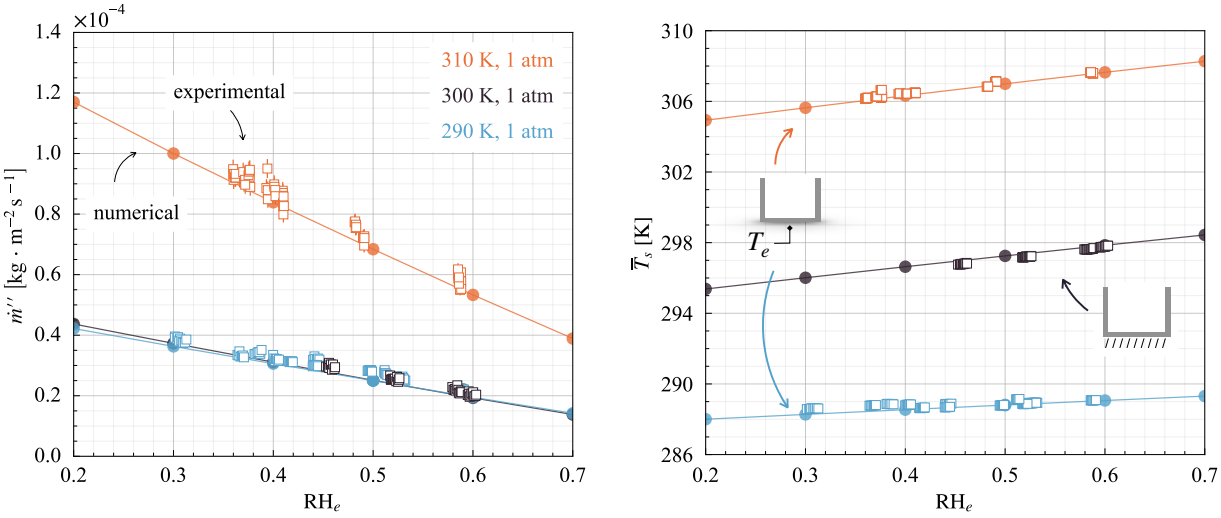

Figure 2.4: Mass flux and temperature of the air-water interface as a function of relative humidity for water evaporating into air under downward flow motion. Three different ambient conditions are evaluated: 290 K (blue), 300 K (gray) and 310 K (orange), all at 1 atm. In the 300 K and 1 atm case, the experimental setup is arranged so as to have the bottom of the container exposed to the surrounding flow motion (zero flux), while in the other cases the bottom is fixed at the ambient temperature T_e. The good agreement between numerical and experimental results indicates the consistency of the energy balance at the interface (Eq. 2.12g) and of the thermal condition offered by the container. The error bars associated to the experimental data (often covered by the markers in this plot) indicate 2 standard deviations.

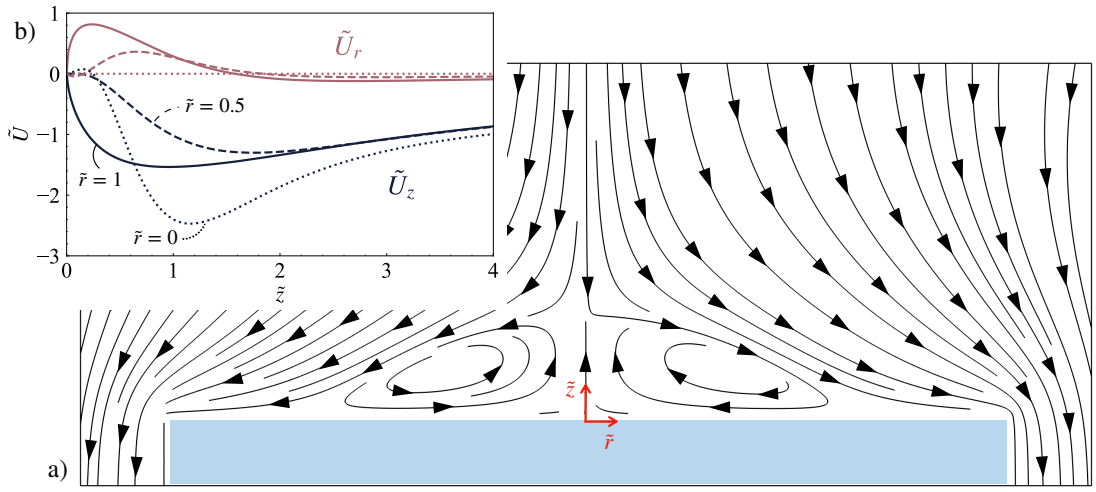

Figure 2.5: Flow structure for water evaporating into air under dominant downward flow motion. a) Streamlines of the flow above the interface with the presence of a stable recirculation zone where both the vertical and horizontal velocity components near the surface are of the same order of magnitude. b) The dimensionless velocity profile of both horizontal, $\tilde{U}_r = u_r/(\nu/R)$, and vertical, $\tilde{U}_z = u_z/(\nu/R)$, components at different radial positions (center, middle and edge), in dimensionless coordinates, $\tilde{r} = r/R$. The horizontal component of velocity is zero at the center, while toward the edge both components are of similar magnitude for distances smaller than 1 radius from the interface. At a height of 4 radii, the vertical component of the velocity is considerably more negative and the flow is almost downward vertical.

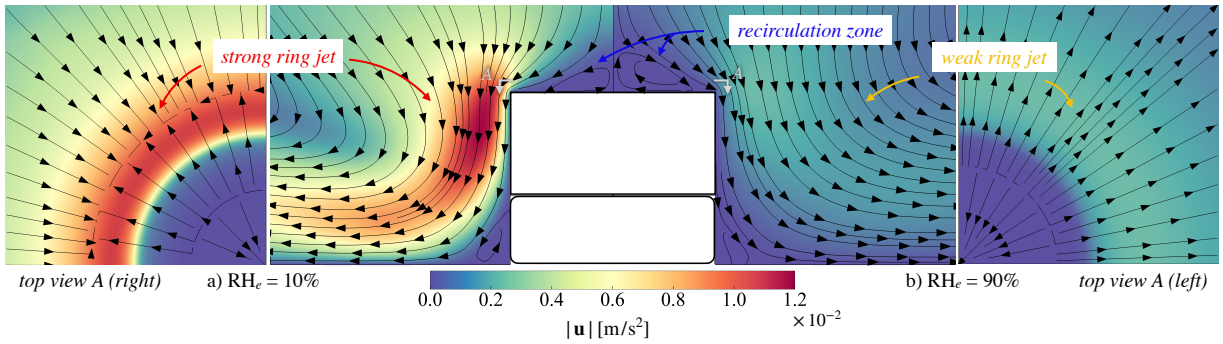

Figure 2.6: Toroidal (ring-like) jet formation around the pool for water evaporating under dominant downward flow motion. Streamlines and velocity magnitudes are shown for evaporation at $T_e = 300\,\mathrm{K}$ and a) $\mathrm{RH}_e = 10\%$ and b) $\mathrm{RH}_e = 90\%$. The high mass flux near the edge of the pool induces lower temperatures near the rim. The result is a downward motion of the air that is accelerated around the walls of the pool. This acceleration generates a toroidal jet structure. For drier free-stream conditions, the air is drawn towards the the rim of the pool from above (stronger ring jets). Such effects becomes weaker under wetter free-stream conditions, causing weaker ring jets.

motion. For the case of an isothermal system with the evaporating surface being a disk, Dollet and Boulongne [17] found a correlation for the Sherwood number consisting of a power law term plus a constant term, $Sh \approx \frac{\pi}{2}(0.31Gr^{1/5}+0.48)$. According to these authors, the two terms result from the difference in local flux contributions along the interface. Once opposing buoyant forces take place, the flow is no longer necessarily upward. For the regimes studied here, the flow is mostly driven downward with the saturated air leaving by the edges. There are also possible stagnation points appearing close to the interface, as shown in Figure 3.4. Stagnation points can be a characteristic of natural flows adjacent to horizontal surfaces undergoing opposing thermal-concentration buoyant effects. The numerical results thus suggest that the horizontal and vertical components of the velocity have the same order of magnitude next to the interface (see

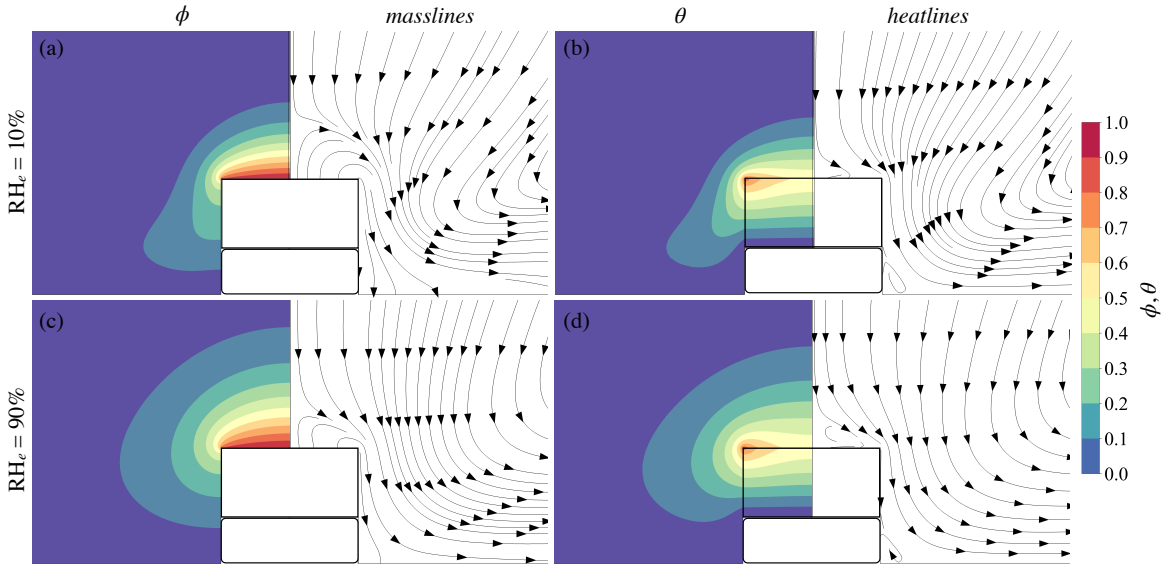

Figure 2.7: Isolines for thermal and mass concentration profiles along with the masslines and heatlines for water evaporating into air under downward flow motion. Results are given for RH$_e$ equal to 10 % and 90 % with T_e at 300 K. The surface of both the thermal and mass concentration gradients approach mushroom-type shapes, which are deformed under buoyant forcing. Under dry conditions (a, b), the high mass flux near the edge induces an intense sinking motion of the air near the rim, that in turn pulls down the isolines around the wall resulting in an enhanced evaporation rate. At high relative humidities (c, d), the flow strucuture is relatively the same, however with a less intense effect. Notice that, near the air-water interface, the pattern of mass and heat flows resembles more the pattern of the recirculation zones when in a wet environment, indicating that under such condition the mass and heat fluxes at the interface are more susceptible to disturbances of the recirculation zones.

Figure 3.4.b) and, for this reason, the boundary layer approach is not applicable [37, 44].

The stagnation points appearing next to the interface are associated to flow reversal or recirculation zones. The recirculation zones appear when the flow accelerates downward, creating a flow structure that resembles a toroidal ring-like jet near the rim of the pool. The downward accelerated flow is induced by the sinking motion of air, as a result of the low temperature near the rim. A more detailed analysis shows that the temperature varies along the air-water interface due to the nonuniform radial mass flux [15, 16]. Because mass fluxes are higher near the edge, a significant lower temperature drop is expected in those locations. Yet, the resulting temperature of the edge depends on how efficiently heat can be transported to that region, which in turn depends on the thermal resistance of the fluid and of the container [38]. It is possible that in the present study the interface is indeed coldest at the rims, since the thermal conductivity of the very thin-walled (<1 mm) container is lower than the thermal conductivity of liquid water ($k_{\text{container}} \approx 0.3 - 0.4\,\text{W}\cdot\text{m}^{-1}\text{K}^{-1}$). The colder air near the rim sinks to the bottom or base of the pool, which is at a slightly higher temperature, resulting in the aforementioned local acceleration of the flow. Such flow patterns then sustain the overall downward motion of the air in the near and far flow stream. An example of such ring-like jet structure encircling the recirculation zones is presented in Figure 2.6 for the evaporation process at $T_e = 300\,\text{K}$. In drier environments ($\text{RH}_e = 10\%$), air is drawn from the above towards the top edge of the pool (strong ring jet), creating a local acceleration of the flow. Such pulling induced motion becomes weaker ($\text{RH}_e = 90\%$) in a wet environment, that nonetheless still produces higher flow velocities near the rim (weak ring jet). As expected, the recirculation zone has a reduced size in the presence of the strong ring jet when compered to the wet condition, in which the recirculation zone is larger.

Figure 2.7 shows how the spatial distribution of temperature and water vapor concentration are affected by the overall flow. The Bejan's masslines and heatlines [27] representing the respective net flow of mass and heat transport are also depicted. The isolines are given in terms of the dimensionless mass concentration ϕ and the dimensionless temperature θ, both defined in

equations 2.18 and 2.19:

$$\phi = \frac{m_1 - m_{1,e}}{m_{1,s} - m_{1,e}}, \tag{2.18}$$

$$\theta = \frac{T - T_e}{T_s - T_e}, \tag{2.19}$$

while masslines and heatlines are respectively given as

$$\frac{\partial M}{\partial z} = u m_1 - \mathscr{D}_{12} \frac{\partial m_1}{\partial x} \tag{2.20a}$$

$$-\frac{\partial M}{\partial x} = w m_1 - \mathscr{D}_{12} \frac{\partial m_1}{\partial z} \tag{2.20b}$$

and

$$\frac{\partial H}{\partial z} = \rho c_p u T - k \frac{\partial T}{\partial x} \tag{2.21a}$$

$$-\frac{\partial H}{\partial x} = \rho c_p w T - k \frac{\partial T}{\partial z} \tag{2.21b}$$

At lower relative humidities, the mass driving force is stronger due to a higher mass concentration difference, and as such more energy is required for evaporation to occur. A more pronounced cooling effect near the air-water interface induces higher thermal gradients, at the same time that it intensifies the sinking motion near the rim. The isolines are then pulled downward around the walls of the pool in consequence of the stronger downward flow. As the relative humidity increases, the flow structure is relatively the same, however less intense and having a more protruding recirculation zone. Notice how, near the air-water interface, the pattern of the masslines and heatlines are more aligned to the shape of the recirculation zone in a wet

environment than in a dry environment, indicating that in such condition the mass and heat flows are likely more sensitive to any effect consequent from disturbances of the recirculation zone.

Despite the downward acceleration locally induced near the edge of the air-water interface, which at first suggests that the evaporation rate is dependent on the effective height of the pool, numerical and experimental results show that a universal correlation can be developed to estimate the evaporation of water under downward flow motion, regardless of the geometrical aspect ration H/R. To evaluate an universal correlation, we conducted experiments with H/R ratios from 0.6 to 1.7, while the ratio was extended to cover values from 0.3 to 5 in the numerical simulations. By using the form of equations 2.17a and 2.17b to perform a fit on the numerical results, we found the following Sh-correlation:

$$\overline{Sh}_R \approx 2 \tag{2.22a}$$

for $Gr_R \leq 10$, and

$$\overline{Sh}_R = 1.73 + 0.26\, Sc^{1/3} Gr_R^{1/4} \tag{2.22b}$$

for $10 < Gr_R < 10^5$.

The Sherwood number is represented in Figure 2.8 in terms of the absolute value of the total Grashof number, $|Gr_{R_m} + Gr_{R_T}|$. For the sake of simplicity, we suggest for Grashof number values less than 10, the approximation $\overline{Sh}_R \approx 2$, which is the value expected in the pure diffusion limit. For Gr values higher than 10, we correlate the Sherwood number to the 1/4 power on the Grashof number. The experimental values are virtually within ±10% of the nominal correlation result, as seen through the region represented by the shaded area around the suggested curve. The proposed correlation is additionally compared to the one proposed by Sparrow et al. [42], also developed for free evaporation with a downward flow motion and Grashof numbers ranging from 10^4 to 10^6. Both correlations initially agree for Grashof numbers around 10^4, but they slightly

diverges as the Grashof number increases, due to the difference in the power on the Grashof number. While Sparrow et al. [42] suggests $Sh \propto Gr^{0.205}$, the correlation proposed here preserves the characteristics of a buoyant laminar flow, besides maintaining the contribution from pure diffusion.

The simplified liquid pool approximation (where buoyancy and surface tension are neglected) yields consistent agreement across the range of experimental conditions described here. The good agreement between the numerical simulations and the experiments, particularly with

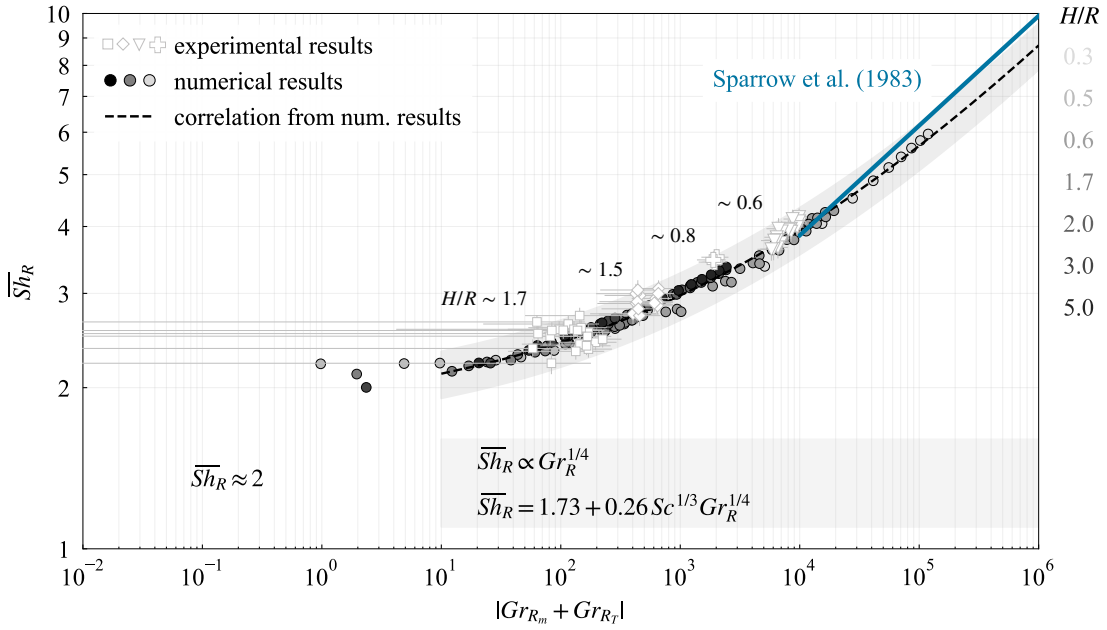

Figure 2.8: Sherwood number as a function of the total Grashof number for water evaporating into air under downward flow motion. Experimental results are conducted for Grashof numbers between 50 and 10^4. The corresponding error bars indicate 2 standard deviations. The numerical results are expanded to cover Grashof numbers from near 1 to 10^5. The Sherwood number approaches 2 for Grashof numbers less than 10, consistent with the expected in the pure diffusion limit. As the Grashof number increases, the flow velocity also increases, leading the Sherwood number to become proportional to $Gr^{1/4}$ - as it is expected for unbounded natural evaporation. The results take into account different geometrical aspect ratios H/R, in turn demonstrating the correlation to be independent of the effective height of the pool. When compared to the correlation proposed by Sparrow et al. (1983) - in which the Sherwood number is proportional to $Gr^{0.205}$, both correlations initially agree at Grashof numbers around 10^4, but they start to slightly diverge as the Grashof number increases due to the difference in the respective powers. Flow recirculations for Gr numbers below 100 are unstable and can only be achieved numerically under idealized boundary conditions.

respect to the air-water interface temperature, corroborates the use of the hydrostatic condition in our simulations. This happens because the general downward flow on the air-vapor side is not affected by the simplified liquid pool model as long as the average heat flux from the liquid to the air-liquid interface is correctly estimated. Multiple simulations comparing the solution with buoyancy terms in the liquid pool at different pool bottom temperatures with simulations considering a hydrostatic pool with virtually conduction heat transfer only reveal that the simplified hypothesis results in heat transfer rates to the interface that differ by 2% or less. Nonetheless, the strength and the exact position of the circulation zone highlighted in Fig. 5 may be affected by consideration of other boundary conditions at the bottom of the pool given the weak convective flows in this problem.

The suggested Sh number correlation is also compared to the correlations for upward convection as provided in Figure 2.9. In order to obtain all the correlations according to the same

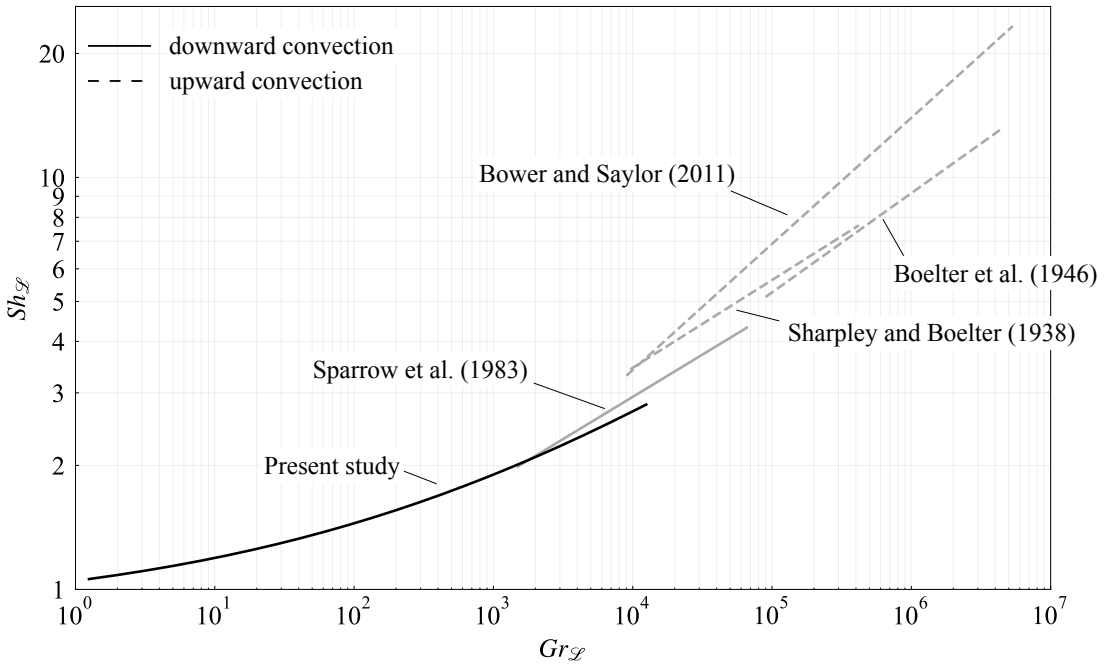

Figure 2.9: Comparison among several Sh number correlations for downward (straight lines) and upward (dashed lines) convection. The correlations obtained from previous studies were converted to the same characteristic length (hydraulic diameter) for comparison. For upward convection correlations the power-law exponent n may differ due to turbulence effects and air-water interface conditions that depend on the heat flow input to the liquid pool.

characteristic length, the correlations were converted to Sh and Gr number values based on the hydraulic diameter, $\mathscr{L} = A/P$, where A is the area of the interface and P is the corresponding perimeter. The correlations corresponding to the upward convection cover in general ranges of $Gr_{\mathscr{L}}$ number of the order of magnitude from 10^4 to 10^6. For upward convection, the Sh number is in general given as a power law function where the obtained power n differs in each study, varying from 0.213 for Sharpley and Boelter [39] to 0.306 for Bower and Saylor [9, 10]. Such variation is likely to be the result of turbulence effects that appear as the liquid pool is heated and alters the dynamics of water vapor transport away from the interface [9, 10].

The relative contribution from the heat fluxes present in the energy balance at the interface (Eq. 2.12g) to the total energy of vaporization is nearly independent of environmental conditions. It does, however, depend on the thermal condition of the container, as shown in Figure 2.10.

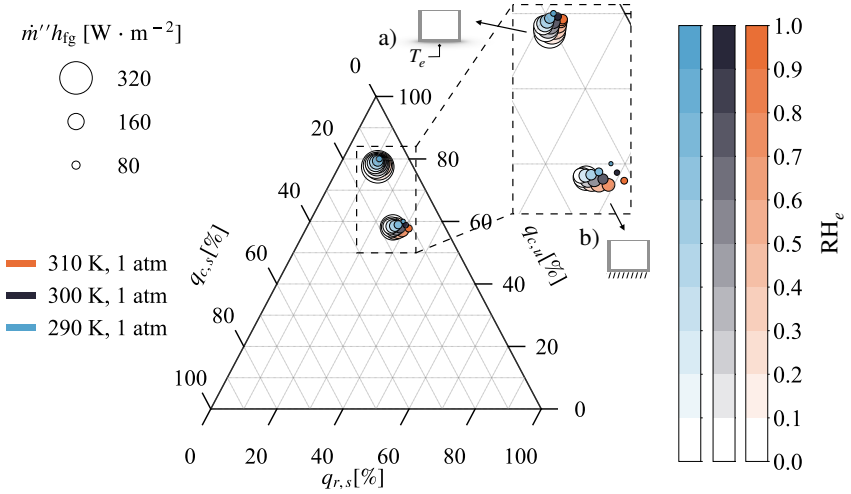

Figure 2.10: Heat flux contribution from numerical results for water evaporating into air under downward flow motion. Each term in the energy balance (see equation 2.12g) is evaluated by varying the RH$_e$ at three different ambient conditions: 290 K (blue), 300 K (gray) and 310 K (orange) - all at 1 atm. The relative contributions are influenced by the thermal condition of the container, which in this study was analysed by changing the thermal condition at the bottom. For instance, when the temperature of the bottom is fixed at the ambient temperature (condition a), the heat flux from the liquid $q_{c,u}$ accounts for approximately 80% of the total heat flux, while the heat flux from the gas $q_{c,s}$ and from radiatiation $q_{r,s}$ share similar parcels of 10% each. When the condition of the bottom becomes zero flux (condition b), $q_{c,u}$ reduces to approximately 60%, while $q_{r,s}$ increases to around 25%, and $q_{c,s}$ to 15%. Overall, the relative contribution from each transport mechanism is virtually the same regardless of environmental condition.

When the bottom of the container is fixed at the temperature T_e, the heat flux from the liquid accounts for approximately 80% of the total required energy, while the heat flux from the gas side and from surface radiation are responsible for relative amounts close to 10% each. Consequently, the heat flux from the liquid is the dominating term. As shown by the results from the three different environmental conditions presented (290 K, 300 K and 310 K, all at 1 atm), the relative contributions to the total energy of vaporization stays virtually the same, regardless of the environmental condition. When the thermal condition at the bottom of the container changes to zero flux, the heat flux from the liquid remains as the leading term, but now having a reduced relative contribution: the heat flux from the liquid in this case accounts for approximately 60% of the total energy, as the contribution from the gas and from surface radiation increase to 15% and 25%, respectively. As expected, the heat fluxes coming from the gas side and from radiation are enhanced as the energy input through the bottom of the container is lowered.

2.6 Concluding Remarks

Free evaporation of water into air from a small-scale circular pool for low Grashof numbers under dominant downward flow motion is examined. Repeatable experiments performed at atmospheric pressure for air temperatures at 290 K, 300 K and 310 K and relative humidity values ranging from 30% to 60%, are described and compared to detailed Finite Element Method (FEM) numerical simulations. For the free evaporation regimes considered here, a downward thermally-induced flow originated at the rim of the pool overcomes the concentration-induced buoyancy, consequently forcing the far-stream warm dry air to descend into the lower temperature air-water interface. Experimental results show that a steady-state recirculation zone near the air-water interface develops for Gr numbers greater than or equal to 50. The Sherwood number for this geometry appropriately scales with $Gr^{1/4}$ for drier free-stream boundary conditions, while it approaches a constant value for smaller mass transfer potentials (i.e., more humid environments).

A stable Sherwood number correlation as a function of Gr values is proposed, covering Gr values from 10 to 10^5.

Chapter 2, in full, is a reprint of the material as it appears in Pool Evaporation Under Low Grashof Number Downward Convection 2021. Medrado, J. P. T.; Inman, R. H.; Coimbra, C. F. M., International Journal of Heat and Mass Transfer, 181, 2021. The dissertation author was the primary investigator and author of this paper.

Chapter 3

Isothermal free evaporation from open tubes

Open tube evaporation processes are ubiquitous in laboratory settings [45, 40], biological systems [1, 5] and engineering applications [51, 41, 53, 52, 54]. When asked to estimate evaporation rates from test tubes, most science and engineering practitioners resort to the classical Stefan diffusion tube, a simplified 1-D binary model where the background (or solvent) species is stationary. Conditions required for an accurate application of Stefan diffusion tube are often not met, specially for processes involving free evaporation from open tubes. In free evaporation from open tubes, strong buoyancy effects induces a multi-dimentional flow structure that in turn leads to a multi-phase regime as the process switch over dry and wet environment conditions.

Natural convection driven by the free evaporation from open tubes under isothermal or near-isothermal conditions is here investigated, using detailed numerical models to solve for the full coupled nonlinear conservation of mass and momentum equations. The validated numerical simulation allows for the analysis of the Sh-Gr curve behavior in the pre- and post-critical regimes. Relative humidity from 0 to 99% and the near-ambient conditions of 1 atm pressure at 290 K and 310 K temperatures are in this way investigated for aspect ratios varying from 2 to 11.

A Sh number correlation is developed for isothermal and near-isothermal open tube evaporation valid in a range of Gr 50 to 4000. The correlation covers all regimes observed under NCTP and is composed by functions representing the behavior of the critical Sh and Gr numbers in terms of the aspect ratio as well as expressions for Sh under the convection driven regime.

3.1 Problem description and method of solution

When natural evaporation occurs, the temperature at the air-water interface decreases compared to the surroundings due to evaporative cooling, or the liquid molecules adjacent to the interface that continuously looses thermal energy to the ongoing phase-change process. Consequently, the natural occurrence of isothermal evaporation is virtually inhibited. Yet, an external energy input to the system combined with a reduced thermal resistance between the air-water interface and the surrounding for processes with a low driving potential (NCTP) can induce the evaporation process to occur under near-isothermal conditions. For example, the approach of minimizing the thermal resistance was applied by Sparrow and Nunez [43] in their study of isothermal open tube evaporation. They used a container made of aluminum with a thin wall (i.d. = 3.80 cm, o.d. = 4.12 cm). Likewise, McBain et al. [30] used a thin wall tube (i.d. = 3.49 cm, o.d. = 3.64 cm) made of polycarbonate walls and an aluminum base, with the purpose of enhancing the amount of energy flowing from the surrounding to the air-water interface and thereby mitigate the interfacial temperature drop. In both studies, an external energy was not forced into the system. Yet, Sparrow and Nunez [43] and McBain et al. [30] observed sufficiently small temperature drop in their respective experiments, which allowed them to consider a quasi-isothermal evaporation process.

Here we too examine an isothermal system where water evaporates from an open tube. Pressure and relative humidity values far away from the air-water interface are known. Due to the slow nature of the natural evaporation process, we assume the process to be in quasi-steady

state. A solution is obtained for each combination of temperature, pressure and relative humidity imposed to the system. Because of the near-ambient condition, the mass transfer driving potential inducing the removal of water vapor away from the interface is sufficiently small ($\delta m_1 < 0.1$) to allow us the use of the low mass transfer rate theory (no blowing at the interface) and a laminar flow condition. The mass, momentum and species conservation equations at the gas side are respectively

$$\nabla \cdot \mathbf{u} = 0\,, \tag{3.1}$$

$$\mathbf{u} \cdot \nabla \mathbf{u} = -\frac{1}{\rho_g} \nabla P + \nu_g \nabla^2 \mathbf{u} + g\, \beta_m \Delta m_1\, \hat{\mathbf{k}}\,, \tag{3.2}$$

$$\mathbf{u} \cdot \nabla m_1 = \mathscr{D}_{12} \nabla^2 m_1\,, \tag{3.3}$$

where P is the pressure including the gravitational potential, $P = p + gz\rho_g$, and β_m is the mass volumetric coefficient of expansion as defined in the appendix. The subscript 1 denoting species 1, refers to the water vapor.

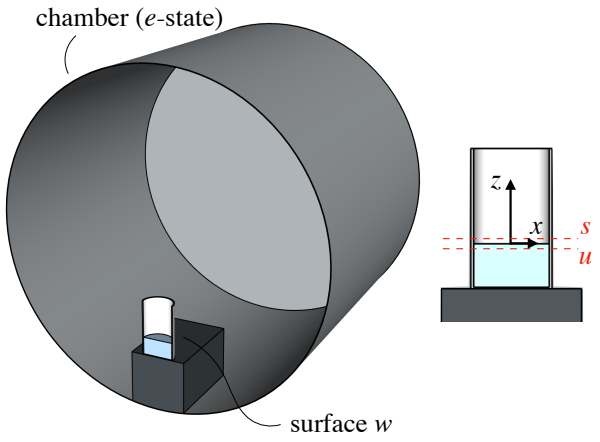

Figure 3.1: Schematic representation of the geometry used in the numerical model along with the coordinate system of reference whose origin is at the center of the air-water interface. The inside of the chamber is seen through its plane of symmetry, the z-x plane, the same plane where a slightly tilt on the gravitational field is applied to only give the fluid flow a preferred direction to establish the anti-symmetric flow. Also depicted is the s and u surfaces representing the air-water interface at the air side and water side respectively, along with the boundaries referring to the e-state (delimited by the walls of the chamber) and the w surface (the walls of the tube).

The governing equations are subjected to the following boundary conditions:

$$\mathbf{u} = 0\,, \tag{3.4a}$$

$$m_1 = m_1\left(\mathrm{RH}_e,\, T_e\right)\,, \tag{3.4b}$$

$\forall\, x \in e,\ \forall\, y \in e$ and $\forall\, z \in e$, where e refers to the boundary representing the e-state (see Fig. 3.1). At the air-water interface:

$$u_x\ (z = 0^+) =\ u_x\ (z = 0^-)\,, \tag{3.5a}$$

$$u_y\ (z = 0^+) =\ u_y\ (z = 0^-)\,, \tag{3.5b}$$

$$u_z = 0\,, \tag{3.5c}$$

$$\mu_g \frac{\partial u_x}{\partial z}\bigg|_{z=0^+} =\ \mu_l \frac{\partial u_x}{\partial z}\bigg|_{z=0^-}\,, \tag{3.5d}$$

$$\mu_g \frac{\partial u_y}{\partial z}\bigg|_{z=0^+} =\ \mu_l \frac{\partial u_y}{\partial z}\bigg|_{z=0^-}\,, \tag{3.5e}$$

$$m_1\ = m_1\left(P_{\mathrm{sat}},\, T_e\right), \tag{3.5f}$$

$\forall\, x \in s,\ \forall\, y \in s$ and $z = 0$, where s represents the air-water interface at the air side, while u, the air- water interface at the water side. Notice that the normal velocity at the interface is set to zero, instead of the velocity due to the balance of convective and diffusive flow resulting from the impermeability of air into water, that is

$$u_z = -\frac{1}{1 - m_{1,s}}\mathscr{D}_{12}\frac{\partial m_1}{\partial z}\bigg|_s\,. \tag{3.6}$$

Including the normal velocity in the model had virtually no effect for the *Sh-Gr* curve. The largest observed difference was for the point correspondent to the condition 310 K, $\mathrm{RH}_e = 0$ (the largest $\mathscr{B}_{m_1}$ analysed here), where the difference was only 2%. For lower temperatures and higher relative humidity values (hence lower $\mathscr{B}_{m_1}$), the difference observed between the models diminishes even further, as expected. We therefore reinforce that the blowing effect for evaporation processes under NCTP can be neglected, as it imparts little change in the solution. We should, however, reframe the importance in accounting for the tangential velocity at the interface induced by the convective cell emerging inside the tube for evaporation under the convection driven regime. Even though a rigid interface can also give accurate results for processes at around the critical *Gr* number [30], the results for a dry condition (near RH_e=0) might be significantly affect by the imposition of a rigid interface. The parameter $\mathscr{D}_{12}$ is the diffusion coefficient of water vapor in air [34] (see C). The mass concentration of species 1, m_1, depends on the saturation pressure, here obtained according to the Tetens equation [46] (see B). Zero mass flux is applied at the walls of the container exposed to the gas side:

$$\nabla m_1 = 0, \tag{3.7}$$

$\forall\, x \in\ w$, $\forall\, y \in\ w$ and $\forall\, z \in w$.

The governing equations and boundary conditions were implemented numerically using the finite element method based software COMSOL Multiphysics. The domain, as shown in Fig. 3.1, was meshed using tetrahedral elements where the region surrounding the interface was comparatively more refined. Results between nodes were estimated according to third order polynomial shape functions. Similarly to McBain et al. [30], the model was first solved for a transient-state with prescribed temperature, relative humidity and pressure. The initial velocity was set to zero, while initial concentration of species 1 (water vapor) defined according to the prescribed relative humidity. In order to excite the anti-symmetric flow mode inside the tube, the gravitational field was tilted one degree from the vertical direction to the right (positive x). The result obtained from this first transient simulation was subsequently used in a steady-state model

Table 3.1: Mesh independence study for numerical simulation of isothermal free evaporation from open tubes. The average Sherwood number is evaluated according to the number of triangular elements at the air-water interface and total dregrees of fredom (DOF).

Total DOF	Triangles	$\overline{Sh}_L$	diff.
214,999	38	11.070	-
454,522	75	11.168	0.9%
801,225	149	11.221	0.5%
1,355,662	296	11.255	0.3%

with equal prescribed values of temperature, relative humidity and pressure, but without a tilt in the gravitational field. In both transient and steady-state simulations, the governing equations were fully coupled, with all the unknowns being simultaneously solved in each iteration through the parallel direct linear solver. The non-linearities of the governing equations were handled by the damped Newton-Raphson method, while streamline and crosswind stabilization methods were used to prevent numerical instabilities. A mesh study for $AR = 8$ for $T = 310\,\mathrm{K}$ and $\mathrm{RH}_e = 0$ was carried out by consecutively refining the air-water interface. As shown in Table 3.1, increasing the number of triangles at the interface to values greater than 75 has insignificant effect upon the dimensionless mass transfer rate. As such, all models were simulated based on an air-water interface having 150 triangles.

3.2 Results and discussion

Here we discuss the mass transport dynamics associated with the free evaporation of water from an open tube under isothermal and near-isothermal conditions. We specifically investigate the dependence of the evaporation rate on the *AR*, a value referent to the distance from the air-water interface to the open-end of the tube. Overall, we consider evaporation processes occurring for *AR* between 2 to 11, at the temperatures 290 K and 310 K and relative humanities ranging from 0 to 99%.

3.2.1 Model validation

The accuracy of the present numerical model is assessed by comparing the obtained solution to the experimental results of Sparrow and Nunez [43] and McBain et al.[30].

McBain et al. [30] carefully carried out an analysis of the isothermal evaporation of water into air, in which they recovered the dimensionless evaporation rate in a wide range of Gr numbers for a tube having an AR equal to 4. In their work, the exact temperature of the experiments is not specified, and a mean of controlling the temperature is not present. Conversely, the authors indicate that the study focused on the evaporation at low mass transfer rate (which normally occurs for temperatures lower than 50 °C), suggesting that the experiments were conducted at ambient conditions. Nunez and Sparrow [43] investigate the isothermal evaporation for various

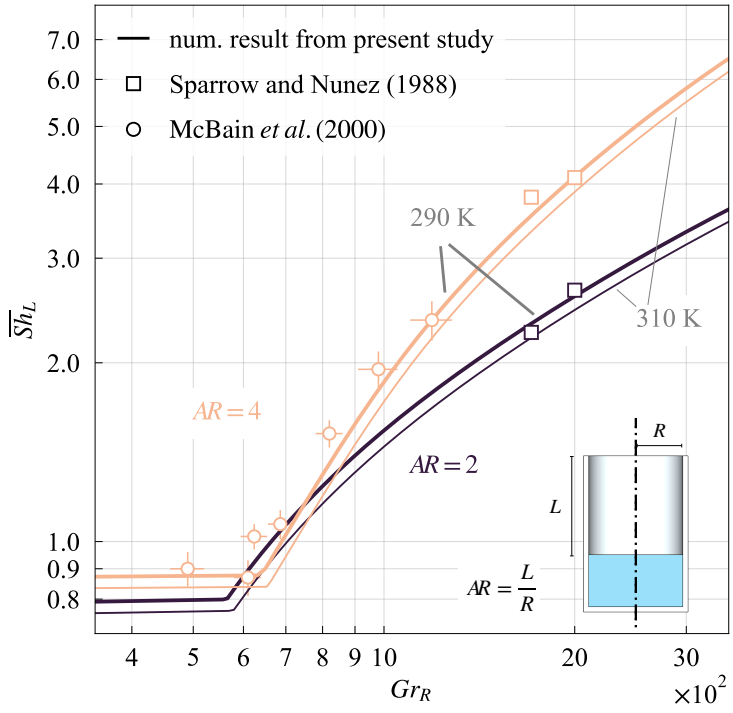

Figure 3.2: Validation of the numerical simulation with the experimental data for the isothermal free evaporation from open tubes. The experimental data are depicted by the square (Sparrow and Nunez 1988) and circular (McBain et al. 2000) markers, while the numerical simulation is represented by the straight thicker (290 K) and thinner (310 K) lines. The experimental values are recovered for AR equal to 2 and 4 in the entire range of Gr number analysed here, indicating the accuracy of the numerical simulation.

AR, including *AR* equal to 2 and 4. Each *AR* was evaluated according to constant values of the Gr number, specifically at Gr_R number (Gr number based on the radius) equal to 1708 and 2000. In both studies, the experiments were performed with a shell container, that is, a container with thin walls (Sparrow and Nunez used a 0.32-cm thick container, while McBain et al. adopted a 0.15-cm thickness). A container with thin walls reduces the thermal resistance between the energy being transferred from the surroundings to the interface. A lower thermal resistance, in turn, reduces the temperature drop resulted from the phase change therein.

In order to fully cover the experimental conditions of Sparrow and Nunez [43] and McBain et al. [30], we numerically simulated the evaporation from a container with thin walls (more specifically, we simulated a container composed by shells with zero thickness since there is not temperature variation during the simulated process and the thickness of the container's wall is vanishingly small compared to the entire gas domain) at the temperatures of 290 K and 310 K, all at 1 atm. The numerical simulation is presented in Fig. 3.2 along with the experimental data from both authors. Our numerical simulation recover the evaporation rate at low (negligible dependence of Sh number on the Gr number) and high (strong dependence of Sh number on the Gr number) Grashof numbers under ambient conditions, therefore being in agreement with the experiments. As seen in Fig. 3.2, the Sh-Gr curves show a slight dependence on temperature, a quality discussed later in this study. We follow with the analysis of the Sh-Gr curve at the 290 K and 310 K temperatures, with *AR* from 2 to 11, for a shell tube.

3.2.2 Evaporation from an open tube in the pure diffusion limit

In pure diffusion, the evaporation rate is dependent only on the concentration differences of the evaporating species. McBain et al. [30] developed a Sh-expression for the pure diffusion limit, based on the analysis of an equivalent potential field created by a point source with cylindrical coordinates as $r = 0$ (center of the container) and $z = H$ (height of the container), while a point sink at $r = 0$ (center of the container) and $z = -H$ (the symmetrical point to H

based on a symmetrical plane defined at the base of the container). They arrive at the equation $Sh_0 = H/(0.594 + H)$ for $Gr = 0$. If the distance to which the potential field extends is of the same order of magnitude as the separation of the point source and point sink, such approximation becomes inappropriate. An ideal potential field equivalent to the evaporation from a circular surface bounded by vertical walls (open tube evaporation) would be the one created by parallel plates capacitors (instead of point sources) of equal magnitude but opposite charges, separated by a distance $2(H - AR \cdot R)$ with a boundary from the source to the height $AR \cdot R$ having zero flux, and the center of symmetry located at the base of the container. Such analysis is, however, beyond the scope of this study.

Although the approach used by McBain et al. [30] might not be entirely valid for all geometrical configurations, the expression they arrive at reveals a compelling characteristic of open tube evaporation: the asymptotic behavior of the Sh number, for which the Sh number asymptotes to an upper limit as the AR increases. We may recall that when AR is vanishingly small, the open tube evaporation becomes pool evaporation, where the mass concentration of water vapor in form of spheroids (mushroom-like shape) are much more evident [31]. In this case,

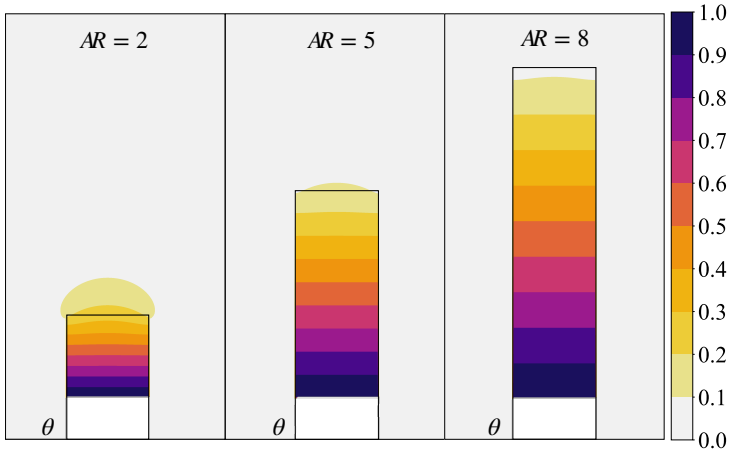

Figure 3.3: Water vapor concentration gradient distribution for pure diffusion at various aspect ratios. For small aspect ratios, the gradient distribution approaches a spheroidal profile near the open-end. As the aspect ratio increases, the gradient distribution gradually turns into a comparatively more linearly stratified profile, however still carrying a circular outline (cap) at the top of the tube.

the isolines of mass concentration in pure diffusion are spread along the external sides of the container. As the *AR* increases, the pool evaporation turns into open tube evaporation and the spheroidal profile of the mass concentration approaches a quasi-linear stratified distribution, with the isolines now confined along the internal walls. To illustrate, Fig. 3.3 shows how the water vapor concentration first forms a spheroidal cap near the open end of the container for *AR* equal to 2 to then progressively flatten, leading to a comparatively more linear concentration gradient as *AR* increases. The overall result is a Sh_L number (the *Sh* based on the distance *L* - see Fig. 3.2) that asymptotically approaches the unit when increasing the *AR*.

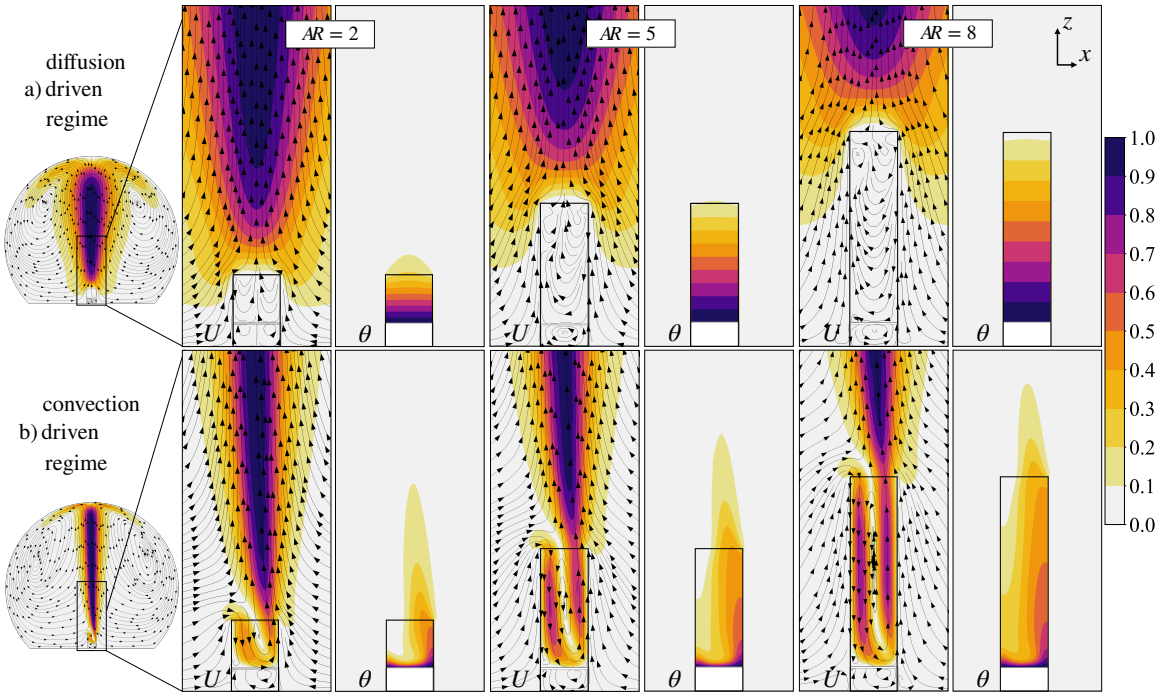

Figure 3.4: Fluid flow and mass concentration gradient profiles for the open tube evaporation, according to the normalized velocity $\tilde{U}$ and water vapor concentration ϕ. In the diffusion driven regime, the fluid flow is insignificant to the mass concentration gradient, whereas in the convection driven regime, the mass concentration gradient is compressed and stretched at opposite sides of the container, following the diametrically anti-symmetric pattern of the flow.

3.2.3 Natural convection in open tubes driven by free evaporation

In the presence of gravitational forces, natural convection induced by thermal and concentration gradients enhances the evaporation rate. Such an enhancement depends on the buoyancy strength and, for open tube evaporation, the buoyancy strength can be classified according to a diffusion or convection driven regime [30].

For Gr numbers near zero, the Sh number starts out from the pure diffusion value, weakly increasing as the Gr number increases (diffusion driven regime). It then reaches a critical Gr number where it shifts to the convection driven regime. Figure 3.4 shows the fluid flow and concentration gradient associated with both diffusion and convection driven regimes, according to the respective normalized velocity $\tilde{U}$ (normalized according to the maximum velocity in the domain) and normalized concentration gradient, $\phi = m_1 - m_{1,e}/m_{1,s} - m_{1,e}$. In the diffusion driven

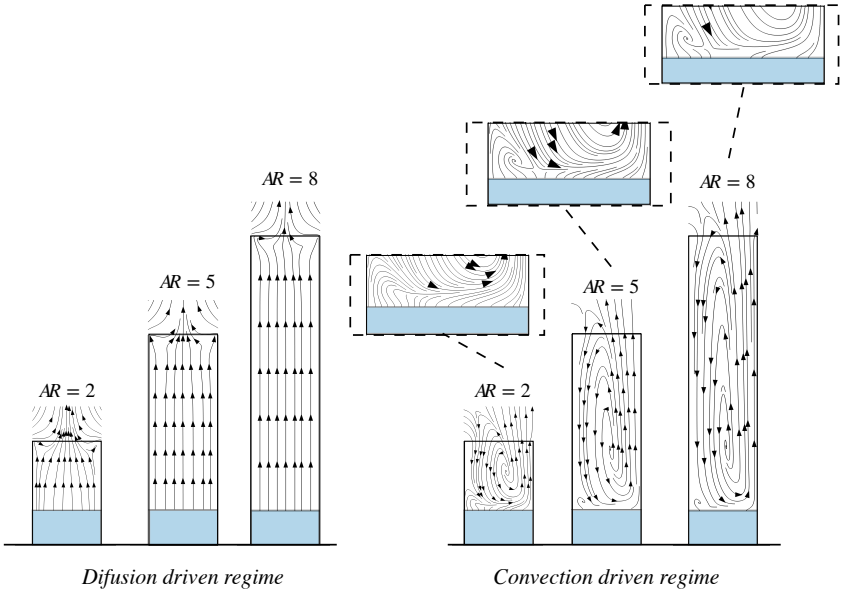

Figure 3.5: Patterns of the masslines for the isothermal open tube evaporation, for the diffusion driven and convection driven regimes at various aspect ratios. In the diffusion driven regime, the net flow of water vapor nearly follows a straight line towards the open-end with virtually no entrainment from the surrounding. In the convection driven regime, on the other hand, a significant entrainment of water vapor is present in one side of the tube. The entrainning water vapor flows towards the air-water interface, where it mixes with the newly formed water vapor. The mixing is carried away from the interface, exiting the container in the opposite side to the entrainment, following the single convection cell pattern.

regime, the flow inside the container is symmetric for $AR = 2$, becoming non-symmetric for higher AR values. For all AR, the flow under the diffusion driven regime has an insignificant effect on the concentration gradient, as the gradient profiles still resemble the ones observed in pure diffusion. On the other hand, the fluid flow in the convection driven regime plays a crucial role on the distribution of the concentration gradient [30] and consequently on the net transport of water vapor. The flow enters the container from one of its side and leaves through the subsequent side, ultimately leading to a simultaneous compression and elongation of the concentration gradient at opposite sides of the tube. Because of the strong convection, the net mass transport is also altered

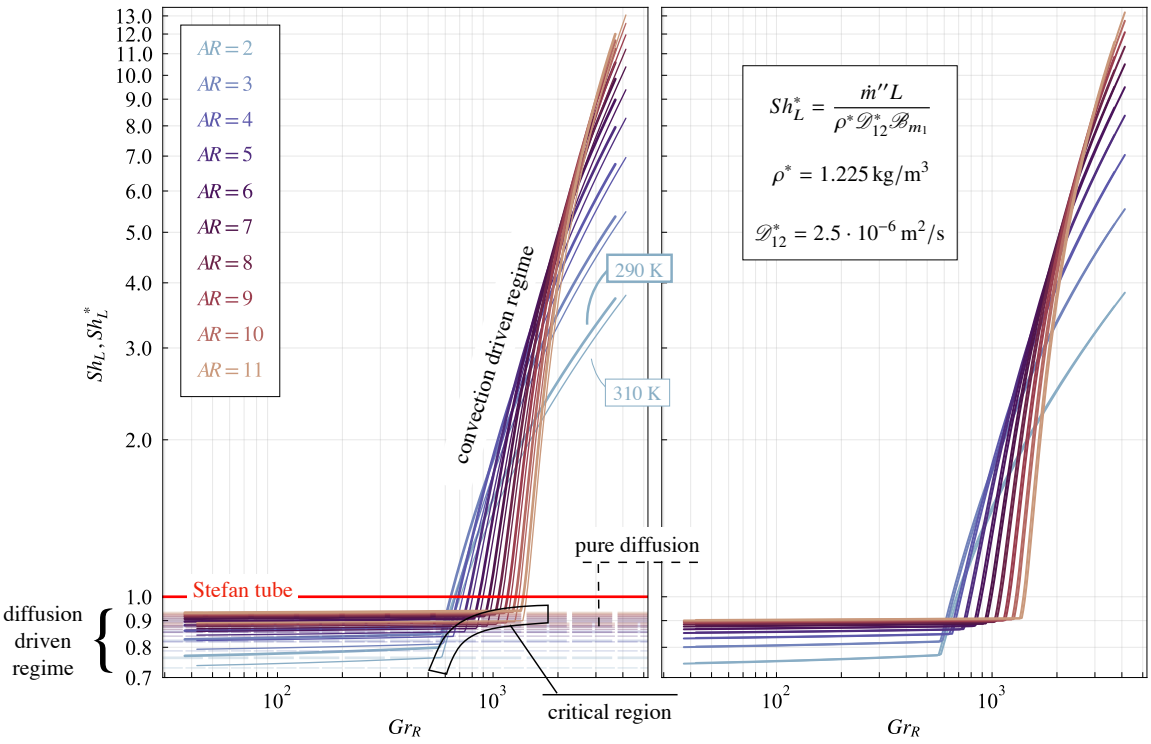

Figure 3.6: Sh-Gr curve for open tube evaporation at various AR for 290-K (thicker line) and 310-K (thinner line) e-state temperatures. The Sh number approaches the pure diffusion value as the Gr number goes to zero. The Sh number increases slightly with Gr number until a critical region that separates the diffusion-driven regime from the convection-driven regime. The 290 K and 310 K curves are slightly shifted in respect to each other in the y-axis due to the temperature dependence of ρ and $\mathscr{D}_{12}$ (left plot). The curves collapse to a single curve when normalized values of ρ and $\mathscr{D}_{12}$ are used (right plot). The Stefan tube model, also displayed (red line), overpredicts the Sh number by up to almost 30% in the diffusion driven regime, while significantly underpredicting the Sh number in the convection driven regime.

in such a way that the configuration of the masslines closely follow the fluid flow pattern. Such fluid flow establishes the diametrically anti-symmetric flow with a single convection cell for all AR.

The masslines of water vapor reflecting the net result of the water vapor transport are shown in Fig. 3.5 for the convection and diffusion driven regimes. While in the diffusion driven regime the masslines nearly follow a straight path with almost no entrainment of water vapor from the surrounding, in the convection driven regime the masslines very closely follow the shape of the single convection cell, with a strong water-vapor entrainment in one side of the tube. At the bottom of the single convection cell, the entraining air mixes with the water vapor originated at

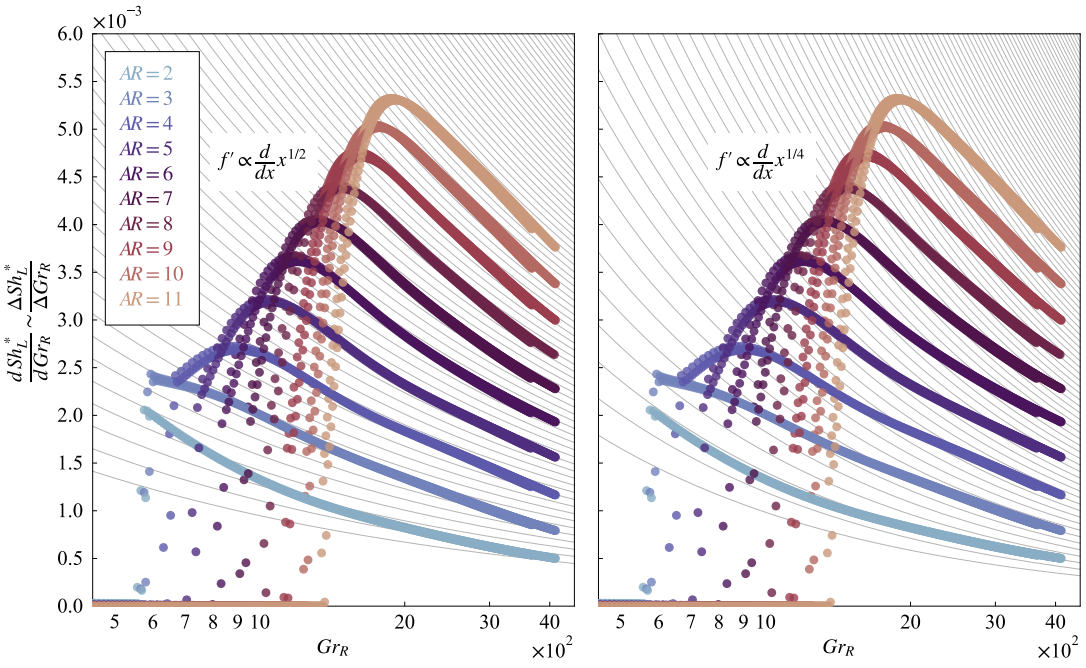

Figure 3.7: Derivatives of the Sh-Gr curves for open tube evaporation, obtained according to the symmetric difference quotient approach. The complex dependence of the Sh number in respect to the Gr number relates to the damping effect caused by the vertical walls bounding the buoyant flow inside the tube. In shorter tubes (AR = 2), inertial terms are favored, which leads to a $Sh \propto Gr^{1/4}$ for all the convection driven regime. As the aspect ratio increases, the evaporation becomes dependent on both the inertial and viscous forces, resulting in a Sh number proportional to $Gr^{1/2}$ and $Gr^{1/4}$. The convection driven regime is also marked by a skewed bell shaped curve, with a peak after the critical point followed by a monotonic decrease characterized by a single oscillation of the curve in this regime.

the air-water interface, forming a mixing-layer. The mixed air flows back to the open-end, exiting the tube to the surroundings.

Figure 3.6 shows the complete Sh-Gr regime for AR varying from 2 to 11. In all the curves, we observe that the change from the diffusion to the convection driven regime occurs as a sudden shift at a specific Gr number (now referred to as the critical Grashof number, Gr_c) as a smooth transition is not present. An important element to the dynamics of the diffusion-convection regime separation is the distance from the air-water interface to the open-end. Overall, the surface area of the walls inhibits the fluid flow motion, hence contributing to the predominance of viscous forces and to the broadening of the diffusion driven regime. As a consequence, the critical Sherwood number, Sh_c, increases with the Gr_c number, following an asymptotic behavior similar to the one observed in the pure diffusion limit. Another important characteristic of the post-critical region (convection-driven regime) is the dependence of the Sh number on different powers of the Gr number. We notice a particular curvature of each Sh-Gr curve in respect to the respective AR value, which is attributed to the interaction between viscous and inertial forces.

Figure 3.6 also shows the Sh number correspondent to the Stefan tube model approach (red line). Because in the Stefan model it is assumed that the boundary condition at the open-end is the mass concentration of the water vapor specified at the prescribed relative humidity value (1-D condition), the concentration gradient reduces to a linear distribution along L for evaporation processes under NCTP. As a result, the Sh number equals 1 regardless of the AR. Except for slender tubes (high AR), treating the concentration gradient as 1-D linearly stratified profile in free evaporation from open tubes can be misleading, even for the evaporation occurring under the diffusion drive regime. In the diffusion driven regime, the Stefan tube overestimates the evaporation rate up to 30% of the actual value when $AR = 2$. The overestimation drops as the AR increases, but as for $AR = 11$ the Stefan tube model still overpredicts the evaporation rate in around 10%. The disparities between the Stefan tube approach and the numerical simulation is even more pronounced in the convection driven regime, with now the Stefan tube underestimating

the evaporation rate: the evaporation rate is up to 13 times (see $AR = 11$) the value estimated from the Stefan tube model.

Regarding the temperature dependence, the curves for the two temperatures (290 K and 310 K) are virtually identical, except for a slight shift in the Sh number. Such a shift results from the dependence of the Sh number on the product $\rho\mathscr{D}_{12}$, where $\rho \propto T^{-1}$ and $\mathscr{D}_{12} \propto T^{1.6}$. When the curves are obtained using nominal values of ρ and $\mathscr{D}_{12}$, the temperature dependence is substantially minimized, as seen in the right plot of Fig. 3.6. Reducing Sh to Sh^* does not compromise the behavior of the curve, and for the sake of simplicity, the analysis that follows is based on the Sh^*. Further details of Sh^*- Gr curve in the convection driven regime is obtained through the analysis of its slope, or its derivative, which eliminates the constant Sh^* value associated with the diffusion driven regime. For simplicity, we will omit the superscript * on the Sh^* number in the rest of this manuscript.

As depicted in Fig. 3.7, the approximated derivative (here taken according to the symmetric difference quotient) shows the complex dependence of the Sh number on both the AR and the Gr number. To highlight the dependence of the Sh number on different powers of the Gr number, also associated to different values of AR, the derivative of the Sh-Gr curve is shown along with derivatives proportional to $f' \propto dx^{1/2}/dx$ (Fig.3.7, left) and $f' \propto dx^{1/4}/dx$ (Fig. 3.7, right), both in gray. These derivatives emphasises the dominance of either the viscous forces (where $Sh \propto Gr^{1/2}$) or inertial forces (in which case $Sh \propto Gr^{1/4}$). From the figure, we notice the rapid increase of the curve towards a maximum value, right after the Gr_c number. The increase to a maximum value is rather a jump as for low AR (AR equal to 2 and 3), or a gradual follow of a skewed bell-shaped curve as in higher AR. After the maximum value is reached, the derivative decreases monotonically, where the dependence of the Sh number on different powers of the Gr number as well as on different values of the AR is evident. The damping effect of the walls is of little importance for $AR = 2$, in which case inertial velocities are dominant and the Sh number proportional to $Gr^{1/4}$. When the AR increases, the damping effect plays a more notorious role,

weakening the velocities near the air-water interface and rising the dependence of Sh number on $Gr^{1/2}$ as well. One can also observe that the Sh number depends on the strength of the Gr number, or more specifically, on the driving potential of a dry, wet or mixed environment. Overall, for AR equal to or less than 2, $Sh \propto Gr^{1/4}$ in the entire convection driven regime. As the AR increases, the Sh number becomes in part proportional to $Gr^{1/4}$ and in part to $Gr^{1/2}$, with each contribution subjected to the AR value.

3.2.4 Sh number correlation for isothermal and near-isothermal free evaporation from open tubes

We first evaluate a representation of the critical region, in order to have the Sh_c and Gr_c numbers expressed as functions of the AR. In Fig. 3.6, the critical points from all curves are highlighted in the area denominated as the critical region. In that figure we see that the critical region suggests that the Gr_c number converges to a lower bound, or that Gr_c number becomes virtually constant for $AR < 2$. A sharp transition from the diffusion to the convection driven regime should vanish for $AR \to 0$, when the buoyant effect is no longer wall-bounded, allowing the Sh number to be expressed according to $Gr^{1/4}$, or a constant Gr number value, depending on the buoyancy strength [31]. In the direction of $AR \to \infty$, the Gr_c most likely finds an upper bound, since that an upper limit for the Gr_c number in closed tube has been already demonstrated [47, 20]. We notice from Fig. 3.6 that for intermediate AR values, the Gr_c number increases with AR. Given all these conditions, a suitable expression to convey the behavior of the Gr_c number is obtained according to a sigmoid function of the form:

$$Gr_{R_c} = a_1 + \frac{a_2 - a_1}{1 + \exp[a_3(AR - a_4)]} \tag{3.8}$$

where a_1 to a_4 are constants to be obtained from a fit to the numerical simulation.

Table 3.2: Estimated coefficients for the proposed correlation of Gr_{R_c} and Sh_{L_c}. The Gr_{R_c} number is represented by a sigmoid function, having lower bound ($a_1 = 450$) and an upper bound ($a_2 = 1667$). The Sh_{R_c} number asymptotes to $\sim 1 + b_2 = 0.94$ as the AR increases, reflecting the non-planar condition of the mass concentration at the open-end, even at high AR values.

a_1	a_2	a_3	a_4	b_1	b_2
450	1667	-0.38	8.22	0.41	-0.06

As previously discussed, the variation of the Sh number is insignificant within the diffusion driven regime, and thus a constant value can be given to express the Sh_c number. In the diffusion driven regime, the Sh_c number also follows a similar asymptotic behavior observed in the pure diffusion limit, which can be expressed as an asymptotic function of the AR as

$$Sh_{L_c} = \frac{AR}{b_1 + AR} + b_2 \tag{3.9}$$

with the constants b_1 and b_2 also obtained from a numerical fit. Finally, we define for the diffusion driven regime

$$Sh_L = Sh_{L_c} \tag{3.10}$$

for $Gr_R < Gr_{R_c}$. The correlations proposed here for the Gr_{R_c} and Sh_{L_c}, obtained by fitting the numerical simulation with the respective equations 3.8 and 3.9 are shown in Fig. 3.8, while the fitted parameters are shown in Table 3.2. From the resulting fit, the lower bound of the Gr_{R_c} number equals 450, while the upper limit is 1667. At very large AR, the critical Sh number asymptotes to 0.94 ($Sh_{L_c} \sim 1 + b_2$) as oppose to unity, reflecting the non-planar surface distribution of the water vapor concentration near the open-end, even at large AR.

To evaluate the convection driven regime, we must take into account the increasing damping effect due to the bounding of the buoyant flow, that eventually leads to the equivalent importance of viscous and inertial forces. As observed in Fig. 3.7, the Sh number becomes proportional to the combined $Gr^{1/2}$ and $Gr^{1/4}$ terms, with the overall dependence conditioned to the AR value. When $AR = 2$, the damping effect is negligible and the entire convection driven

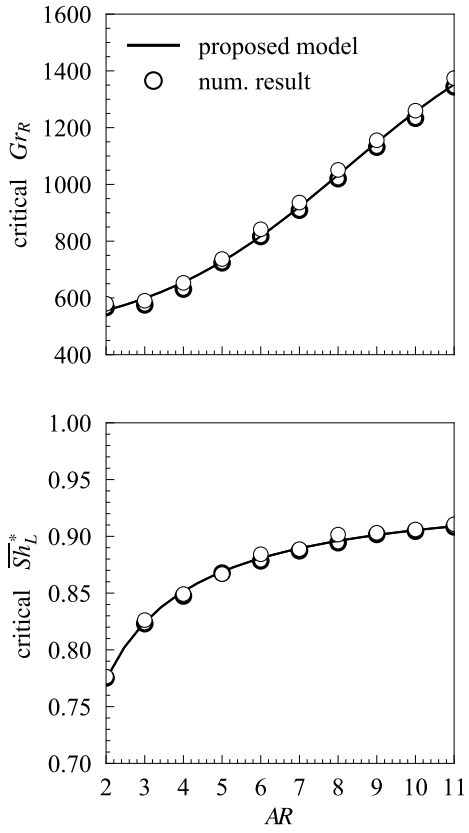

Figure 3.8: Proposed correlation for the Gr_{R_c} and Sh_{L_c} numbers according to equations 3.8 and 3.9, respectively. The numerical simulation for the critical points obtained from the normalized 290 K (thicker edge marker) and 310 K (thinner edge marker) are also shown. The Gr_{R_c} number model is composed by lower and upper bounds as the AR goes to zero and $+\infty$, respectively. The Sh_{L_c} number asymptotically approaches the limit ~ 0.94 as the AR increases.

regime proportional to only $Gr^{1/4}$. For higher AR, the curve rapidly increases to a maximum value after the critical point, to then decrease proportionally to a $Gr^{1/2}$ and $Gr^{1/4}$ combined term. Such consequent behavior from the damping effect due to the presence of walls can be modeled as an exponential function representing a single oscillation,

$$\frac{dSh_L}{dGr_R} = c_1 \exp(-c_2 Gr_R) + c_3 \frac{1}{2} Gr_R^{-1/2} + c_4 \frac{1}{4} Gr_R^{-3/4} , \tag{3.11}$$

Table 3.3: Estimated coefficients for the *Sh* number correlation in the convection driven regime. Except for c_4, which is a constant value, the variables c_1 to c_3 are indeed quadratic functions of the aspect ratio, with the coefficients c_a, c_b and c_c obtained from a fit using the numerical simulation. While c_1 and c_2 describe the maximum value of the instantaneous slope, parameter c_3 reflects the influence of viscous forces and c_4 the inertial force upon the evaporation rate (see equation 3.12).

c_{1_a}	c_{1_b}	c_{1_c}	c_{2_a}	c_{2_b}	c_{2_c}	c_{3_a}	c_{3_b}	c_{3_c}	c_4
-0.0743	0.171	-0.046	2.73×10^{-6}	-9.30×10^{-4}	0.012	2.04×10^{-4}	0.044	-0.080	0.0183

which upon integration gives the following *Sh* correlation:

$$Sh_L = -\frac{c_1}{c_2}\exp(-c_2 Gr_R) + c_3 Gr_R^{1/2} + c_4 Gr_R^{1/4} + c_5 \tag{3.12}$$

for $Gr_R > Gr_{R_c}$. The variables c_1, c_2, c_3 and c_4 are non-dimensional, solely depend on *AR*. They are well expressed according to a quadratic function of the *AR*, that is,

$$c_{1,2,3,4} = c_a AR^2 + c_b AR + c_c \ . \tag{3.13}$$

While the variables c_1 to c_3 are indeed quadratic functions of *AR*, c_4 is rather a constant value,

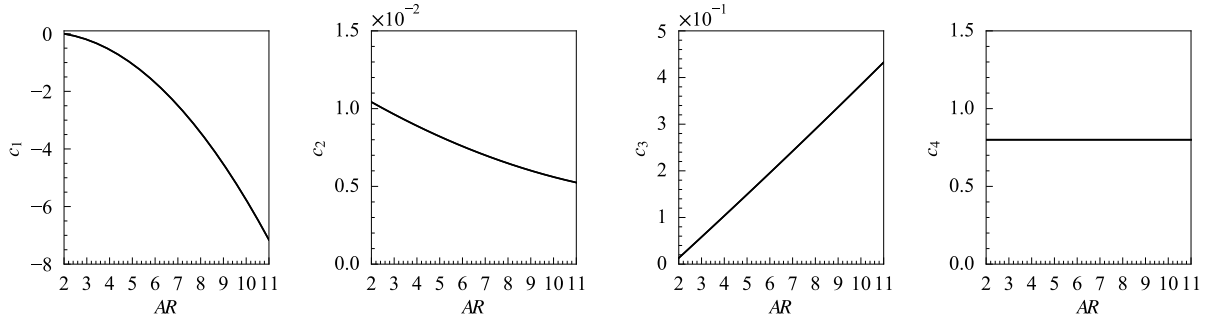

Figure 3.9: Variables c_1 to c_4 for the *Sh* number correlation in the convection driven regime, as quadratic functions of the aspect ratio. The variables c_1 to c_3 associate to the viscous forces and predominates at large *AR*. When *AR* approaches zero, all variables but c_4 vanishes, in which case the correlation (equation 3.12) reduces to a term proportional to $Gr^{1/4}$ plus a constant term, in agreement with pool evaporation (no damping effect due to vertical walls bounding the buoyant flow).

with its $c_a = c_b = 0$.

The variables c_1 and c_2 relate to the peak of the *Sh-Gr* slope. c_3 reflects the influence of the viscous forces, while the variable c_4 is the term correspondent to the importance of inertial forces. Note in Fig. 3.9, where the c-variables are plotted against the AR, that as AR decreases c_1 approaches zero, consequently vanishing the exponential term of equation 3.12. The variable c_3 also approaches zero with the decrease of AR, leaving the variable c_4 as the dominating term for small AR. The reduction of equation 3.12 to a term proportional to $Gr^{1/4}$ plus a constant for vanishing AR values is in agreement with the correlations for pool evaporation [31]. The variable c_5 is obtained as a function of variables c_1, c_2, c_3 and c_4, with equation 3.12 evaluated at the critical point, that is, $c_5 = Sh_L(AR, Sh_{L_c}, Gr_{R_c})$.

Figure 3.10 shows a comparison between the proposed correlation and the numerical simulation for the *Sh-Gr* curve's slope in the convection driven regime. The proposed correlation

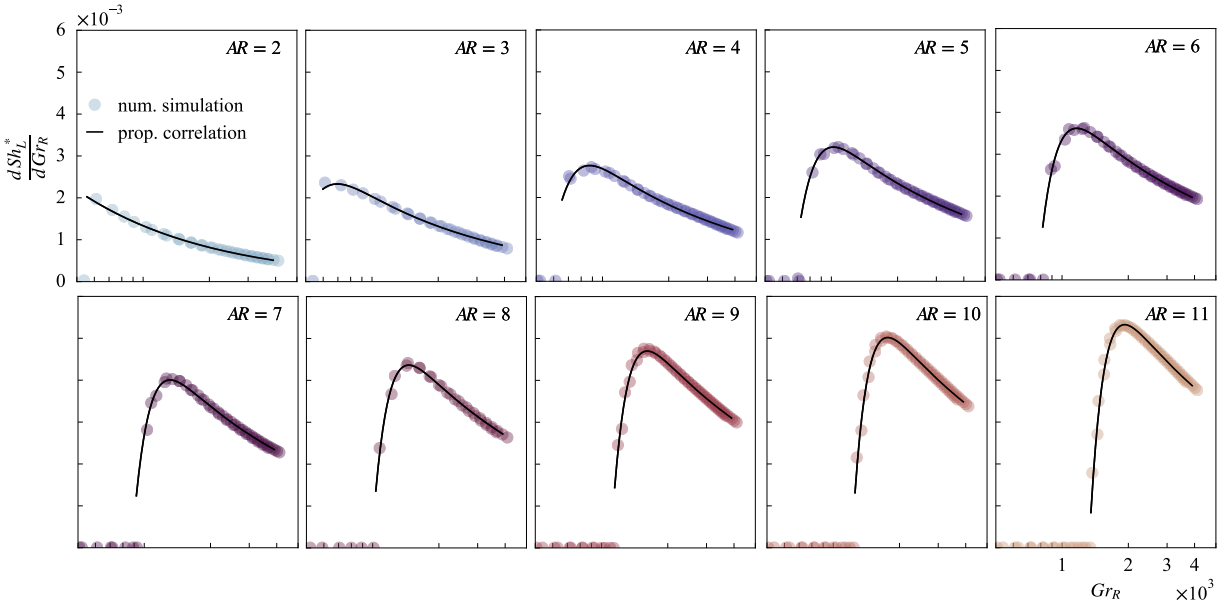

Figure 3.10: *Sh-Gr* curve's instantaneous slope in the convection driven regime according to the numerical simulation and proposed correlation. The proposed correlation reproduces with accuracy the complex variation of the curve that is particular to each aspect ratio, from the sudden jump to the maximum value right after the critical point at low AR to the skewed bell shaped curve for higher AR values.

recovers in detail the complex dynamics of viscous and inertial force interaction, an interaction indeed particular to each *AR*. The suggested model is able to accurately reproduce the sudden change in the *Sh*-*Gr* curve's slope as it transitions from the diffusion to the convection driven regime, as well as the peak followed by the monotonic decrease of the curve. Moreover, the proposed correlation highlights the physical aspect of the evaporation process, emphasizing the overall contribution of viscous and inertial forces that depend on the damping effect due to the bounded buoyant flow. Finally in Fig. 3.11, a comparison of the numerical simulation and proposed correlation for the *Sh*-*Gr* curves is displayed along with the resulting percentage error. We see that for the conditions analysed in this study, the maximum percentage error is virtually within ±5%, for all *AR* investigated under NCTP.

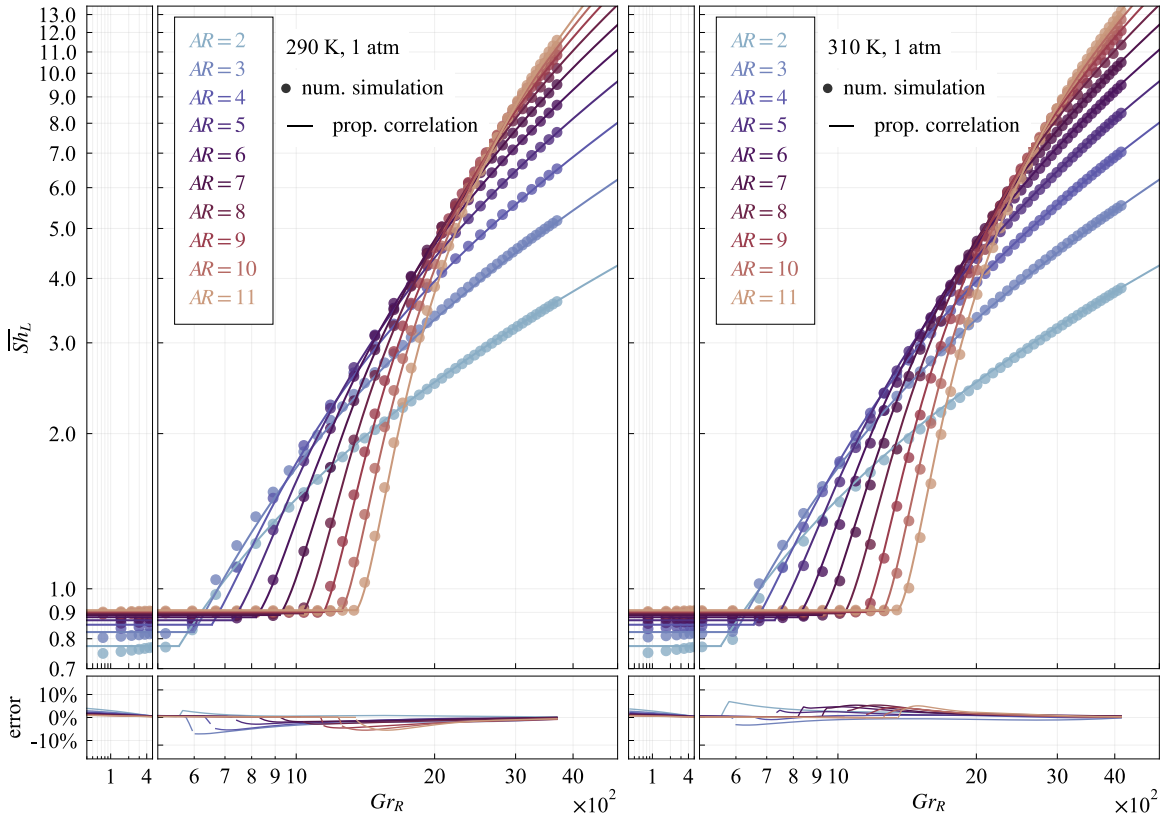

Figure 3.11: Comparison between the numerical simulation and the proposed correlation for the *Sh*-*Gr* curve. The percentage error of the proposed correlation is within 5% for all aspect ratios analysed in this study, reflecting the robustness of the proposed correlation to estimate the free evaporation from open tubes under isothermal or near-isothermal conditions.

3.3 Concluding remarks

The evaporation from open tubes is investigated for isothermal or near-isothermal conditions. The mass transport is overall characterized by complex massline patterns due to the interaction of the vertical walls with the buoyant flow. Using numerical simulations validated by experimental data for typical NCTP, the water vapor transport dynamics is analysed for open tubes with aspect ratios ranging from 2 to 11 and relative humidity values from 0 to 99%, all at 1 atm. The dependence of the diffusion-driven and convection-driven regimes as functions of the geometrical aspect ratio of the tubes is demosntrated. A new Sherwood number correlation valid for both isothermal and near-isothermal processes in the range of Grashof numbers from 50 to 4,000 is proposed. This correlation, which is nearly invariant on temperature as it is normalized according to nominal values of ρ and $\mathscr{D}_{12}$, expresses the Sherwood and Grashof numbers for variying aspect ratios. The proposed correlation estimates evaporation rates within 5% of values obtained from 3-D numerical simulations for the entire range of Grashof and Sherwood numbers under study.

Chapter 3, in full, has been submitted for publication of the material as it may appear in Isothermal and Near-Isothermal Free Evaporation from Open Tubes. Medrado, J. P. T.; Inman, R. H.; Coimbra, C. F. M., International Journal of Heat and Mass Transfer, 2021. The dissertation author was the primary investigator and author of this paper.

Chapter 4

Non-isothermal evaporation from open tubes

Open tube evaporation is a common form of low Grashof number convection. However, the physics underlying this type of flow is not well understood mainly due to the sensitivity of low Grashof number flows to boundary conditions.

Detailed numerical simulations validated against experimental results are used in this work to investigate the dynamics of natural convection driven by free evaporation from open tubes (i.e., low Grashof number flows). Evaporation from tubes having a gas-side aspect ratio equal to 2, 3 and 4 reveals how buoyancy effects present in the gas and liquid domains can culminate in a fully stable system when the onset of convection is induced in the liquid.

4.1 Problem description and method of solution

When water freely evaporates under NCTP, gas and liquid molecules in the vicinity of the interface loose energy to the phase change process, resulting in evaporative cooling. Mass and thermal buoyancy are consequently induced in the gas and thermal buoyancy in the liquid. The

conservation equations governing the steady momentum and energy transfer in the liquid are

$$\nabla \cdot \mathbf{u} = 0 \,, \tag{4.1}$$

$$\mathbf{u} \cdot \nabla \mathbf{u} = -\frac{1}{\rho_l} \nabla P + \nu_l \nabla^2 \mathbf{u} \; + g \; \beta_T \Delta T \, \hat{\mathbf{k}} \,, \tag{4.2}$$

$$\mathbf{u} \cdot \nabla T = \; \alpha_l \nabla^2 T \; . \tag{4.3}$$

The gas, which we considered a binary system formed by water vapor and air, is governed by the following conservation equations:

$$\nabla \cdot \mathbf{u} = \; 0 \,, \tag{4.4}$$

$$\mathbf{u} \cdot \nabla \mathbf{u} = -\frac{1}{\rho_g} \nabla P + \nu_g \nabla^2 \mathbf{u} + g \; (\beta_m \Delta m_1 + \beta_T \Delta T) \, \hat{\mathbf{k}} \,, \tag{4.5}$$

$$\mathbf{u} \cdot \nabla T = \; \alpha_g \nabla^2 T \; , \tag{4.6}$$

$$\mathbf{u} \cdot \nabla m_1 = \; \mathscr{D}_{12} \nabla^2 m_1 \; , \tag{4.7}$$

In both groups of governing equations, P refers to pressure and gravitational potential, $p + gz\rho_g$, a term essentially negligiable in this problem. The respective β_m and β_T are the mass and thermal volumetric coefficients of expansion - see Appendix A. Densities differences in the gas as well as in the liquid are accounted for in the body force term, according to the Boussisnesq approximation.

For the diffusion of energy across the walls of the tube,

$$\nabla T \; = 0. \tag{4.8}$$

The described governing equations are subjected to the following boundary conditions (see Fig.

4.1 for reference):

$$\mathbf{u} = 0 \,, \tag{4.9a}$$

$$T = T_e \,, \tag{4.9b}$$

$$m_1 = m_1 \left(\mathrm{RH}_e, T_e \right) \,, \tag{4.9c}$$

$\forall\, x \in e, \forall\, y \in e$, and $\forall\, z \in e$. Neglecting solubility of air in water under NCTP, we assume that only water vapor is transferred at the interface [32]. Thus, at the air-water interface:

$$u_x \left(z = 0^+ \right) = u_x \left(z = 0^- \right) \,, \tag{4.10a}$$

$$u_y \left(z = 0^+ \right) = u_y \left(z = 0^- \right) \,, \tag{4.10b}$$

$$u_z = 0 \,, \tag{4.10c}$$

$$\mu_g \frac{\partial u_x}{\partial z}\bigg|_{z=0^+} = \mu_l \frac{\partial u_x}{\partial z}\bigg|_{z=0^-} \,, \tag{4.10d}$$

$$\mu_g \frac{\partial u_y}{\partial z}\bigg|_{z=0^+} = \mu_l \frac{\partial u_y}{\partial z}\bigg|_{z=0^-} \,, \tag{4.10e}$$

$$T(z = 0^+) = T(z = 0^-) = T_s(r) \,, \tag{4.10f}$$

$$-\rho_g \mathscr{D}_{12} \frac{\partial m_1}{\partial z}\bigg|_{z=0^+} h_{\mathrm{fg}} + \varepsilon\sigma(T_s^4 - {T_e}^4) = -k_g \frac{\partial T}{\partial z}\bigg|_{z=0^+} - k_l \frac{\partial T}{\partial z}\bigg|_{z=0^-} \,, \tag{4.10g}$$

$$m_1 = m_1 \left(P_{\mathrm{sat}}, T_s \right) \,, \tag{4.10h}$$

$\forall\, x \in s, \forall\, y \in s$, and $\forall\, z \in s$. Finally, for the walls of the tube

$$T = T_{\mathrm{f}}\ , \tag{4.11a}$$

$$\mathbf{n} \cdot q = k_{\mathrm{f}} \nabla T|_{\mathrm{f}}\ , \tag{4.11b}$$

$$\nabla m_1 = 0\ , \tag{4.11c}$$

$\forall\, x \in w, \forall\, y \in w$, and $\forall\, z \in w$.

4.1.1 Numerical method

The finite element solver COMSOL Multiphysics is used to solve the governing equations and boundary conditions. Tetrahedral elements compose the domain of the problem, with mesh elements near the air-water interface more refined. Third order polynomial shape functions interpolate between-node results. As in the work of McBain et al. [30] and Medrado et al. [32],

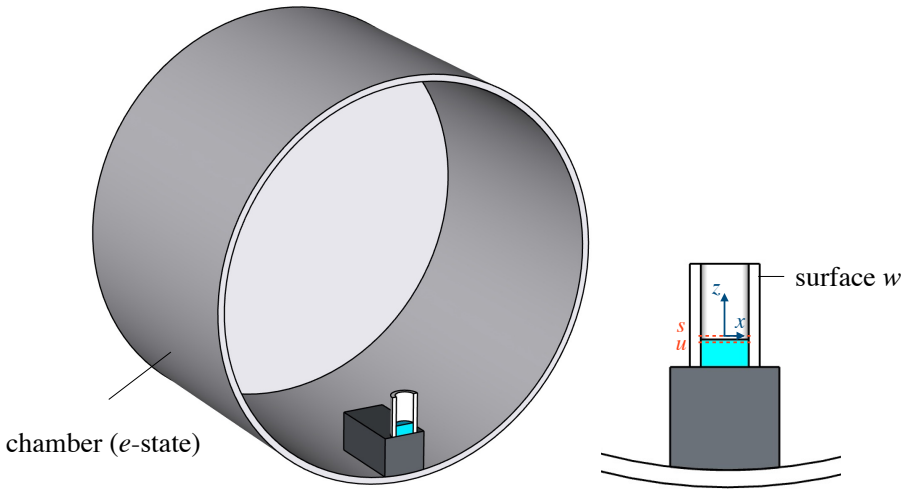

Figure 4.1: Schematic representation of the domain used in the numerical simulation of free evaporation from open tubes. The coordinate system is placed at the center of the interface. The walls of the chamber define the far-stream physical boundary, the *e*-state. The gas-side and liquid side of the interface are respectively represented by surfaces *s* and *u*. The walls of the tube are referred to as the *w* surface.

Table 4.1: Mesh independence study for numerical simulation of non-isothermal free evaporation from open tubes. The average Sherwood number is evaluated according to the number of triangular elements at the air-water interface and degrees of freedom (DOF) for a tube of $AR = 2$. Models having more than 150 elements in the interface shows negligible mass transfer rate change.

Total DOF	Triangles	$\overline{Sh}_L$	diff.
418,215	34	1.8493	-
531,173	73	1.8607	0.62%
827,158	150	1.8618	0.06%
1,381,418	300	1.8623	0.03%

the unsteady state simulation of a given pressure, temperature and relative humidity condition is first solved with a tilted gravitational field to excite the diametrically-asymmetric flow structure under a dry environment. A steady-state simulation of the same boundary-value problem is subsequently solved without the tilt in the gravitational field. The governing equations are fully coupled in order to solve all variables simultaneously — for more details regarding the numerical procedure, see [32].

Table 4.1 shows a mesh independence study for a non-isothermal open tube evaporation where the $AR = 2$. The analysis shows that models having more than 150 elements at the air-water interface produces virtually no change in the mass transfer rate.

4.1.2 Experimental method

A pressure-temperature-humidity controlled chamber defines the far-stream boundary condition of the evaporation process. Thermocouples, a pressure sensor and a hygrometer track the thermodynamic state of the chamber's interior during the process. A 20-mm O.D. and 14-mm I.D. open tube made of polyoxymethylene (POM) is partially filled with water and placed inside the chamber over a high-precision balance. An infrared sensor continuously measures the air-water interfacial temperature. The balance measures the amount of water evaporating during the process, and because the level of water in the tube decreases as evaporation goes on, the entire process is repeated for subsequent targets of relative humidity. In each experimental run, the mass flux is

calculated according to a linear regression based on sub-ranges of mass measurements over time. A χ^2 is applied to determine the number of degrees of freedom to be used in each sub-range of experimental data. Once each data sub-range is defined, the mass flux and the average value of all the other variables are calculated. See [31] for more details of the experimental procedure.

4.2 Results

Here we analyse the natural convection induced by buoyant flows in the gas and liquid. It is specifically demonstrated how convective cells emerge in the system and remain stable during both convection driven and diffusion driven regimes, if the onset of convection occurs in the liquid.

4.2.1 Validation of numerical method

The numerical simulation is validated against experiments performed for non-isothermal free evaporation from open tubes having an AR equal to 2, 3 and 4, with a far-stream temperature fixed at approximately 300 K. The numerical simulation captures the behavior of the mass transfer rate across the evaluated range of relative humidity, a range covering values from approximately 10% to 80%. At such low Grashof number flows (i.e., free evaporation) the mass transfer becomes very sensitive to any disturbance during the evaporation process. For example, we notice that the temperature of the high precision balance measuring the remaining liquid inside the tube is slightly above the average temperature of the chamber's walls ($\sim \Delta T$ of 0.2 K to 0.5 K). To best replicate the conditions of free evaporation during the experiment, we also accounted for such temperature variation. However, effects related to temperature gradient across the walls of the chamber is not considered in the simulation due to the complexity involved. Overall, the numerical simulation reasonably captures the behavior of both evaporation regimes for all aspect ratios under study: the convection driven regime, where the Sherwood number strongly depends

on the Grashof number; and the diffusion driven regime, where the Grashof number's dependence on the Sherwood number becomes negligible.

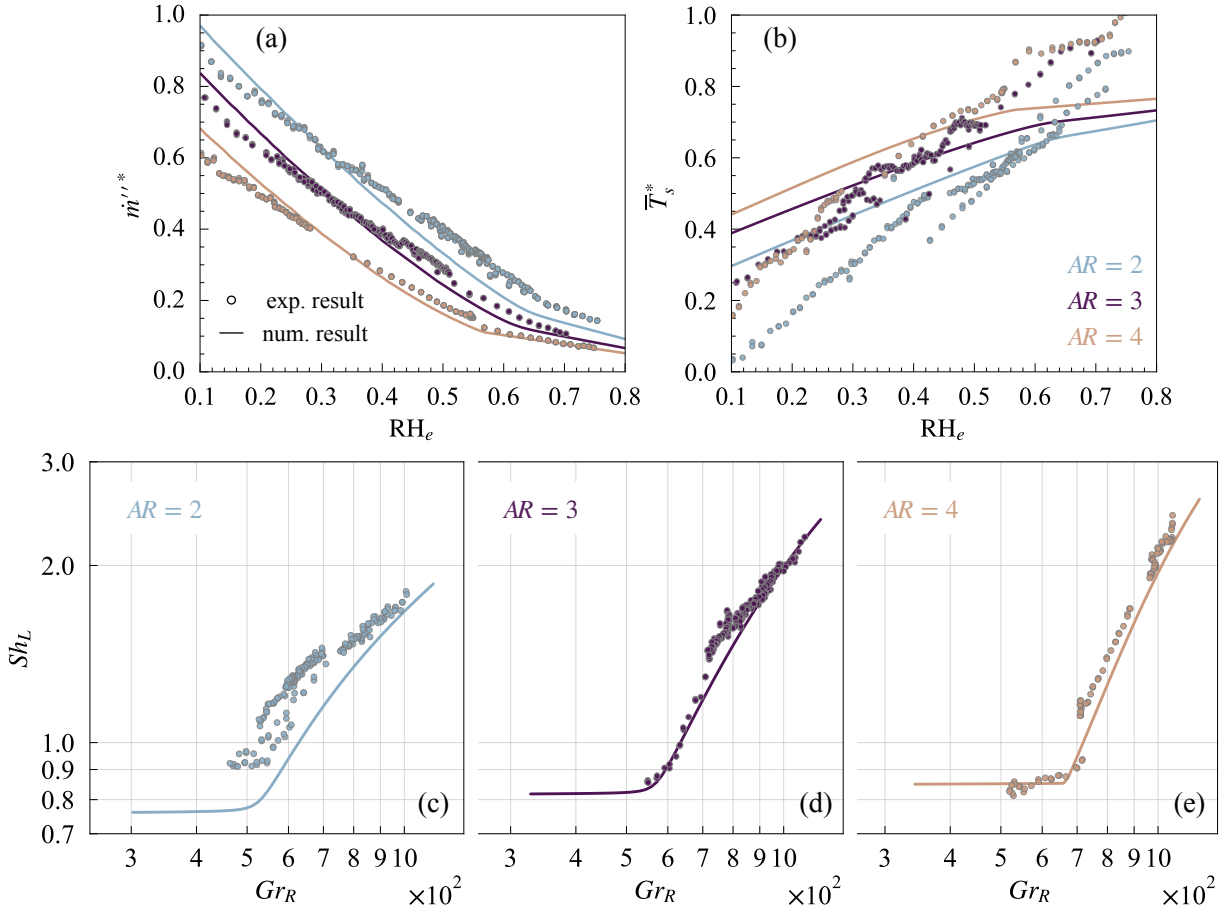

Figure 4.2: Validation of numerical simulations with experimental results for non-isothermal free evaporation from open tubes. The evaporation is analysed for T_e at 300 K, RH$_e$ values from 0.1 to 0.8, and AR equal to 2 (blue), 3 (purple) and 4 (orange). The mass flux (a) and temperature of the interface (b) are parameterized according to nominal values (4×10^{-5} kg/m^{2}s - 0 and 299 K - 300 K). Each corresponding Sh-Gr curve is also shown (c, d and e). In-homogeneous effects such as a weak temperature gradient across the walls of the chamber is likely affecting the experiment. Nonetheless, for all AR the numerical solution captures the behavior of the process, as noted from how the trend is recovered for convection driven and diffusion driven regimes.

4.2.2 Convective flow dynamics in non-isothermal free evaporation from open tubes

In order to emphasize a more general process of free evaporation from open tubes, conditions particular to the experiment such as temperature heterogeneity in the balance were removed. Instead, a homogeneous temperature equal to T_e was considered. The discussion below thus refer to the aforementioned general free evaporation process.

Isothermal evaporation from open tubes occur under two mass transport regimes [30, 32]: the diffusion driven and the convection driven regime. The diffusion regime is characterized by a negligible dependence of the Sh number on the Gr number, and where little or virtually no entraiment of surrounding air into the tube results in essentially straight lines of net water vapor mass transport from the air-water interface to the open-end. In the convection driven regime, the now strong entraiment of air into the tube induces a flow structure composed by a single convective cell in the gas, forcing the lines of net mass transport to follow the convective cell pattern. Moreover, the transition from the diffusion to the convection driven regime for isothermal evaporation occurs at a so called critical Gr number [32]. The stable convective cell once observed in the convection driven regime dissipates under the diffusion driven regime, as it is replaced by a flow structure no longer affecting the masslines of water vapor.

Contrary to the isothermal case, when free evaporation from open tubes occur under non-isothermal conditions, a smoother transition from the convection driven to the diffusion driven regime takes place. The single convective cell in the gas forces an uneven mass flux distribution at the interface. High interfacial mass fluxes are located at the side where the surrounding air enters the tube and descends from the open-end. Uneven interfacial mass fluxes thus result in asymmetrical thermal gradients across the air-water interface for non-isothermal processes. Since here the bottom temperature of the water body is at T_e, which is in general higher than the average T_s, buoyancy consequently develops in the liquid.

For a shallow water body where convection is mostly suppressed, the temperature gradient across the interface has a circular shape with the lowest temperature point localized between the interface's edge and centre, as show in Fig. 4.3. If instead the liquid body is tall enough as to allow for the onset of convection in the liquid, the resulting lowest interfacial temperature moves to the edge or rim of the air-water interface, specifically to the side where the entrainment of surrounding air is established. Under such a distinct interfacial temperature, the cold liquid sinks down along the adjacent container's wall to the container's bottom. As a result, a single convective cell originates in the liquid, oriented according to the described liquid buoyant flow motion.

The rotation of the convective cell emerging in the liquid has an opposite direction relative to the gas-side convective cell rotation. Moreover, the liquid-sided convection dominates the motion prevailing at the air-water interface. A consequence from the opposite convective-rotation of the water side in respect to the air side is the appearance of a dual convective cell structure

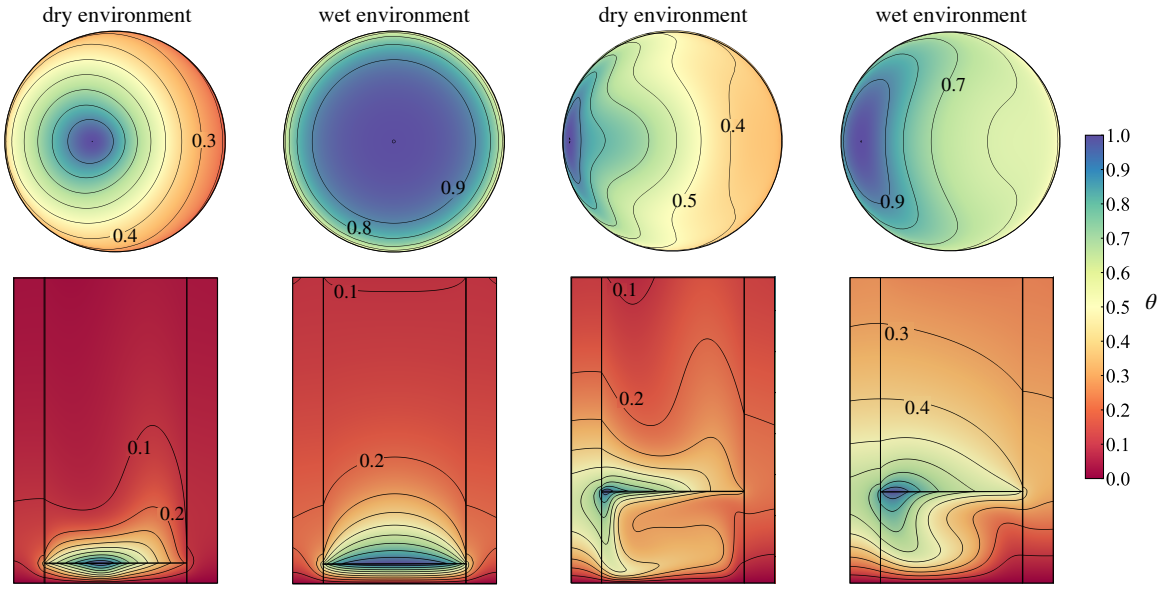

Figure 4.3: Normalized temperature gradient developing in free evaporation from open tubes. The uneven interfacial mass flux distribution induces temperature gradients across the interface. In a system where the bottom of the liquid body is kept at T_e, the evaporative cooling of the interface can result in a weak or strong buoyant motion of the liquid, depending on liquid-side aspect ratio and interfacial temperature drop.

in the gas. While the primary cell results from the strong entrainment of air inside the tube, the secondary cell emerges from the buoyant motion induced in the liquid by the uneven interfacial mass flux distribution. The strong entraiment of surrounding air in the convection driven regime causes the secondary cell to be initially confined into a small region (see Fig. 4.4). As the driving potential decreases and the evaporation process transitions to the diffusion driven regime, the secondary cell grows in size and occupies a larger portion of the gas domain.

When the onset of convection occurs in the liquid, the equilibrium state achieved by the overall flow results in stable cells in both liquid and gas, under either convection driven or diffusion driven regimes. The flow structure that develops under the convection driven regime with an "apparent" single convective cell progressively evolves into the dual cell structure in the diffusion-dominated phase, ultimately resulting in a smooth transition between regimes. If, on the other hand, convection in the liquid side is weak due to, for example, a shallow water body, then a stable cell is only observed for the gas-sided convection driven regime. The once stable cell dissipates in the diffusion driven regime, giving room to a flow structure with virtually no influence on the net transport of water vapor, similarly to the isothermal case. The development of the flow structure is shown in Fig. 4.4 according to five stages of the evaporation process: starting from a flow structure under a dry environment (stage A), followed by a condition in the pre-critical regime and near the critical point (stage B), at approximately the critical Sh-Gr number (stage C), post-critical regime right after the critical point (stage D) and finally in a wet environment condition (stage E). The masslines representing the net transfer of water vapor nearly follows the pattern of the single convective cell in the gas for evaporation processes under the convection driven regime, having either a strong or weak convection in the liquid (stages A and B). When the process transitions to the diffusion drive regime however, the masslines become essentially straight paths of water vapor moving from the interface to the open-end for a weak convection in the liquid (stage C — weak convection in the liquid), similarly to isothermal evaporation from open tubes [32]. This massline pattern remains practically unchanged when further reducing

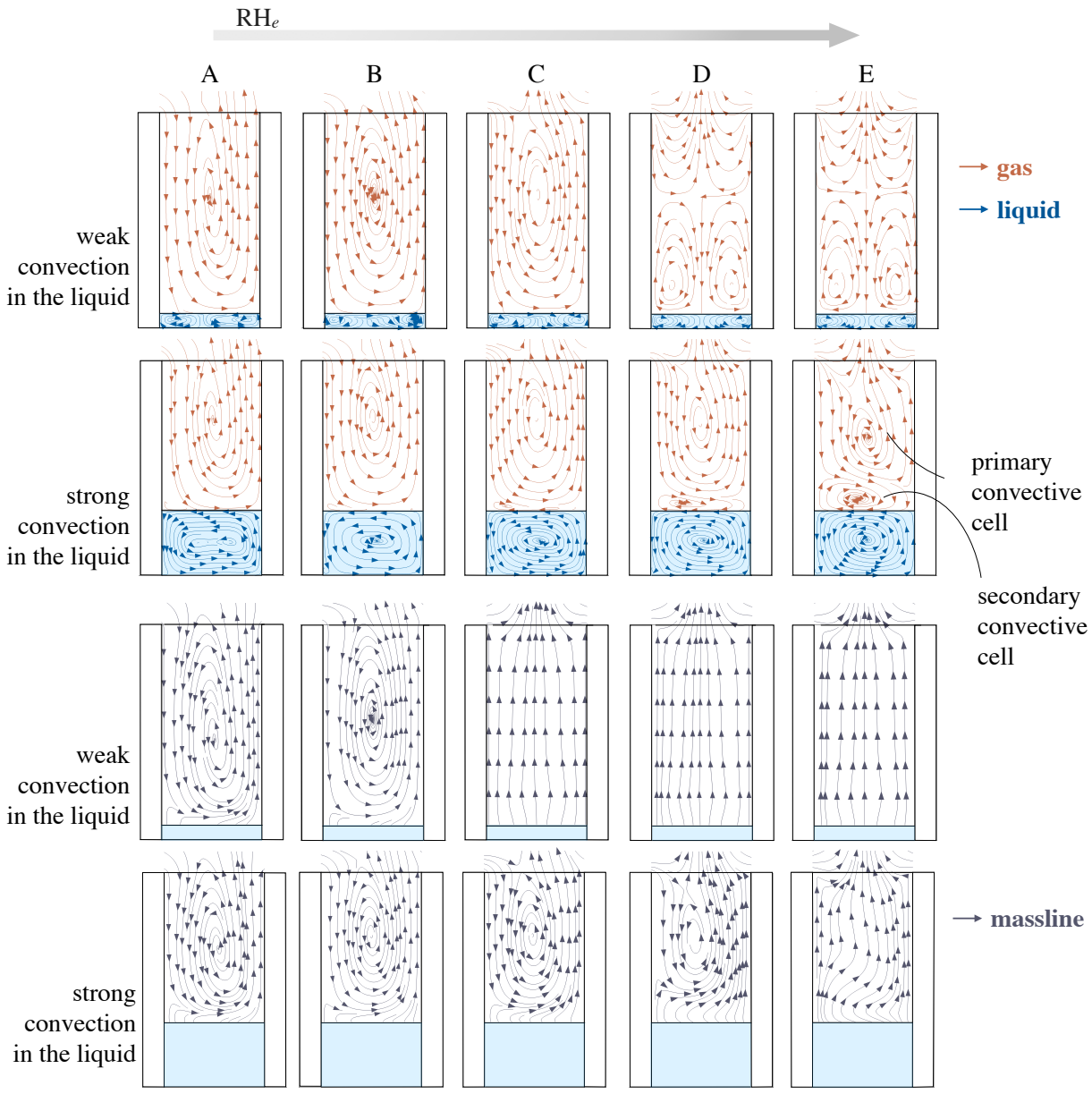

Figure 4.4: Streamlines and massline patterns depicting the flow structure net transport of water vapor at different stages during free evaporation from open tubes. For a weak or strong convection in the liquid, the masslines follow the streamline pattern during the gas-side convection driven regime (stages A and B) as a strong entraiment of surrounding air occurs. When the convection is weak in the liquid, the masslines become essentially straight paths from the air-water interface to the open-end with little entraiment. The masslines are still affected by the convective flow if the onset of liquid convection is induced, resulting in a curved pattern (stage E).

the mass driving potential (stages D and E — weak convection in the liquid). If instead strong convection occurs in the liquid, the masslines originally following the shape of the convective cell in the pre-critical regime (stages A and B — strong convection in the liquid), continue to follow the cell pattern in the critical and post-critical regimes (stages C and D, respectively — strong convection in the liquid) to subsequently change to a skewed pattern when under a wet condition (stage E — strong convection in the liquid).

As mentioned previously, the stable flow structure in non-isothermal evaporation from open tubes causes a smoother transition from the diffusion driven to the convection driven regime when compared to the isothermal case. In Fig. 4.5, where both curves are plotted for comparison, one can observe the sudden switch between regimes for the isothermal curve, while a gradual transition occurs for the non-isothermal condition. Moreover, the Sh number limit in the diffusion driven regime decreases for the non-isothermal case, as also observed in Fig. 4.5. Lower Sh

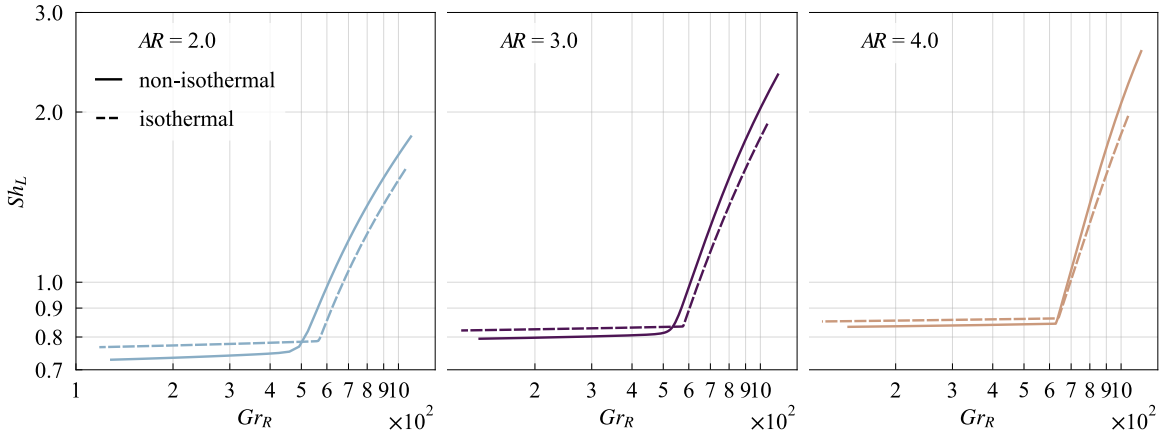

Figure 4.5: Sherwood number as a function of the Grashof number for isothermal and non-isothermal free evaporation from open tubes. The transition from the diffusion driven to the convection driven regime is in general smoother for the non-isothermal case, due to the convective flow structure that remains stable under both regime if the onset of convection occurs in the liquid ($AR_g = 2$, for example). When convection in the liquid is inhibited ($AR_g = 4$), the single convective cell once stable in the convection driven regime dissipates in the diffusion driven regime, resulting in a sharper transition. Moreover, the limit of the Sherwood number in the diffusion driven regime tends to decrease for a strong-convection in the liquid, a consequence of the double convective cell structure, that in general weakens the mass concentration gradient in the gas.

numbers in the diffusion driven regime is likely to be a result from the double convective cell flow structure, that in general reduces the mass concentration gradient inside the tube. When the secondary convective cell grows in size and significantly reduces the kinetic energy of the gas domain (pushing the process to the diffusion driven regime), the continued presence of the primary convective cell induces a higher outflow of water vapor. In terms of the Gr number, the overall temperature reduction of the systems shifts the Sh-Gr curve to lower Gr numbers. When convection in the liquid is strong, the shift is more pronounced (Fig. 4.5, $AR = 2$) then when liquid convection is suppressed (Fig. 4.5, $AR = 4$).

4.3 Concluding remarks

The non-isothermal evaporation from open tubes is studied using numerical simulations in agreement with experimental results for aspect ratios equal to 2, 3 and 4. A detailed analysis of the flow structure shows that, compared to the isothermal case, non-isothermal evaporation is in general characterized by a smoother transition between the diffusion-driven and convection-driven regimes, as convective cells in both liquid and gas is stable for both regimes. This stability is the equilibrium condition achieved by the process when the uneven interfacial mass flux induces the onset of convection in the liquid. When liquid convection is suppressed, on the other hand, the overall flow structure resambles that found in isothermal open tube evaporation processes.

Chapter 4, in full, is currently being prepared for submission for publication of the material. Medrado, J. P. T.; Inman, R. H.; Coimbra, C. F. M. The dissertation author was the primary investigator and author of this paper.

Chapter 5

Conclusions

Free water evaporation processes from small scale circular pools and open tubes are investigated for normal conditions of temperature and pressure. The governing equations are solved numerically and validated against experimental results obtained under a controlled environment, as well as against experimental data available in the literature. The agreement between experiments and theory reinforce the choice of radiative-convective boundary conditions at the air-water interfaces. When present, evaporative cooling effects in these flows result in thermal gradients having opposite direction to mass concentration gradients. These weak gradients on the gas side generate reasonably stable complex patterns at very low Grashof number flows. The gas-sided overall stability allows for a consistent analysis of the evaporation process across a wide range of Grashof numbers. The mass transport is thus systematically analysed, and Sherwood number correlations are obtained for various geometrical configurations.

For free evaporation from a pool with dominant downward motion, the heat flux from the liquid provides the most significant contribution to the total heat of vaporization, although the relative contribution of each transport mechanism depends on the energy supplied to the interface through the bottom of the pool. The vertical and horizontal components of the velocity near the air-water interface are of same order of magnitude, which precludes the use of simplifying

boundary layer approximations in the study of weakly convective flows at low Grashof numbers. Thermal and mass concentration are spherically-symmetric isosurfaces sensitive to disturbances caused by the surrounding buoyant convective forcing. Because of the drop in temperature near the rim of the pool, the cold air sinks and induces a local acceleration of the flow near the rim. Recirculations zones originating at the air-water interface are thus enveloped by the sinking air in a toroidal ring-like jet structure. For wet environments with minimal disturbances, the evaporative process results in a Sherwood number based on the radius of the pool only slightly higher than 2 for Grashof numbers less than 10. This Sh number value is the expected one for the pure diffusion limit. For Grashof number values higher than 10 and up to 10^5, a Sh number correlation is proposed: $\overline{Sh}_R = 1.73 + 0.26\, Sc^{1/3} Gr_R^{1/4}$ for $10 \leq Gr_R < 10^5$. The proposed correlation covers geometrical aspect ratios H/R from 0.3 to 5, while obeying the scaling law associated with unbounded laminar buoyant flows.

The evaporation from open tubes under isothermal or near-isothermal conditions at NCPT is also analysed for aspect ratios ranging from 2 to 11. The evaporation process occurs under two distinct regimes, namely the diffusion driven and the convection driven regimes. In the diffusion driven regime, the Sherwood number is nearly independent of the Grashof number, with the fluid flow having little effect on the concentration of water vapor inside the tube or on the net transport of water vapor away from the interface. In the convection driven regime, where the Sherwood number depends more strongly on the Grashof number, the flow deforms the concentration gradient and alters the conventional straight path of the masslines. A strong entrainment of surrouding air is established at the open-end, while a mixing layer forms near the air-water interface where the entrained air mixes with the newly released water vapor. The transition between regimes occurs at a single point, here denominated as the critical Grashof and Sherwood numbers. The critical Grashof and Sherwood numbers are dependent on the aspect ratio in a way that, increasing the aspect ratio increases both critical values. Such is a consequence of the damping effect due to the walls of the tube bounding the buoyant flow, a result that favors the overall predominance

of viscous forces in the flow. The behavior of the *Sh*-*Gr* curve is particular to each aspect ratio: when the aspect ratio is small, $Sh \propto Gr^{1/4}$; whereas for higher values of *AR*, the *Sh* number becomes proportional to $Gr^{1/2}$ and $Gr^{1/4}$. The slope of the *Sh*-*Gr* curve is characterized by a single oscillation in the convection driven regime. The derivative of the curve in the convection driven regime revels that such an oscillation is in general associated with the wall-damping effect, and is appropriately expressed according to an exponential term. A Sherwood number correlation covering the diffusion and convection driven regimes is suggested for aspect ratios between 2 and 11, at near-ambient isothermal and quasi-isothermal conditions. The correlation is composed by an asymptotic equation representing the Sh_c for $Gr \leq Gr_c$, a sigmoid equation for the Gr_c, and an exponential equation to obtain the *Sh* in the convection driven regime, for $Gr > Gr_c$. The proposed model captures all features observed in free evaporation from open tubes, including the weak oscillation found in the post-critical regime.

When free evaporation from open tubes occurs under non-isothermal conditions, convective cells emerging in the gas and liquid can remain stable during both diffusion-driven and convection-driven regimes. Such stability is the equilibrium condition achieved by the process when the uneven mass flux distribution at the air-water interface excites strong convection in the liquid, ultimately resulting in a smoother transition between regimes. An exception is encountered if convection is suppressed, resulting in a isothermal-like evaporation process instead.

Appendix A

Coefficient of volumetric expansion

The thermal and mass coefficients of volumetric expansion, β_T and β_m, are expressed for a binary mixture as

$$\beta_T = -\frac{1}{\rho}\frac{\partial \rho}{\partial T}\bigg|_{\rho_1, p} \approx \frac{1}{T_e}, \tag{A.1}$$

$$\beta_m = \rho\left(-\frac{1}{\rho}\frac{\partial \rho}{\partial \rho_1}\bigg|_{T, p}\right) \approx \frac{M_2}{M_1} - 1, \tag{A.2}$$

with M being the molecular weight of the species in question. Note that equation A.2 implies $\rho_2 \gg \rho_1$ and $x_2 \gg x_1$. The former is approximately true for water vapor (species 1) in air (species 2), while the latter is always true for the same mixture under tropospheric conditions.

Appendix B

Saturation pressure of water vapor

The saturated vapor pressure in this work is estimated using the Tetens equation [46]

$$P_{\text{sat}} = 0.61078 \exp\left(\frac{17.27\,T}{T+237.3}\right), \tag{B.1}$$

where T is in degrees celsius and P_{sat} is in kilopascals.

Appendix C

Binary diffusion coefficient for water vapor in air

The binary diffusion coefficient of water vapor in air used in this study follows the empirical relation [34]

$$\mathscr{D}_{12} = 1.97 \times 10^{-5} \left(\frac{P_0}{P}\right) \left(\frac{T}{T_0}\right)^{1.685}, \tag{C.1}$$

where $P_0 = 1$ atm, $T_0 = 256$ K and $\mathscr{D}_{12}$ given in $\mathrm{m/s^2}$.

Bibliography

[1] Adlassnig, W., Peroutka, M., and Lendl, T. Traps of carnivorous pitcher plants as a habitat: composition of the fluid, biodiversity and mutualistic activities. *Annals of Botany 107*, 2 (12 2010), 181–194.

[2] Alsaati, A., and Marconnet, A. Energy efficient membrane distillation through localized heating. *Desalination 442* (2018), 99 – 107.

[3] Askounis, A., Takata, Y., Sefiane, K., Koutsos, V., and Shanahan, M. E. R. Biodrop evaporation and ring-stain deposits: The significance of dna length. *Langmuir 32*, 17 (2016), 4361–4369.

[4] Bartlett, D. F., and Corle, T. R. The circular parallel plate capacitor - a numerical solution for the potential. *Journal of Physics A-Mathematical and General 18*, 9 (1985), 1337–1342.

[5] Bartlett-Healy, K., Healy, S. P., and Hamilton, G. C. A Model to Predict Evaporation Rates in Habitats Used by Container-Dwelling Mosquitoes. *Journal of Medical Entomology 48*, 3 (05 2011), 712–716.

[6] Boelter, L. M. K., Gordon, H. S., and Griffin, J. R. Free evaporation into air of water from a free horizontal quiet surface. *Industrial & Engineering Chemistry 38*, 6 (1946), 596–600.

[7] Bourouni, K., Bassem, M., and Chaïbi, M. Numerical study of coupled heat and mass transfer in geothermal water cooling tower. *Energy Conversion and Management 49*, 5 (2008), 988 – 994.

[8] Bourouni, K., Martin, R., and Tadrist, L. Analysis of heat transfer and evaporation in geothermal desalination units. *Desalination 122*, 2 (1999), 301 – 313.

[9] Bower, S., and Saylor, J. A study of the Sherwood-Rayleigh relation for water undergoing natural convection-driven evaporation. *International Journal of Heat and Mass Transfer 52*, 13 (2009), 3055 – 3063.

[10] Bower, S., and Saylor, J. Erratum to "a study of the Sherwood–Rayleigh relation for water undergoing natural convection-driven evaporation" [Int. J. Heat Mass Transfer 52 (2009) 3055–3063]. *International Journal of Heat and Mass Transfer 54*, 1-3 (2011), 749.

[11] Brewster, M. Q. Evaporation of water at high mass-transfer rates by natural convection air flow with applications to spent-fuel pools. *International Journal of Heat and Mass Transfer 116* (2018), 703 – 714.

[12] Chapman, J. D., Kottke, P. A., and Fedorov, A. G. Enhanced thin film evaporation via impinging electrospray liquid jets with entrained air streaming. *International Journal of Heat and Mass Transfer 131* (2019), 1879 – 2189.

[13] Charlson, G., and Sani, R. On thermoconvective instability in a bounded cylindrical fluid layer. *International Journal of Heat and Mass Transfer 14*, 12 (1971), 2157–2160.

[14] Chen, Y. H., Hu, W. N., Wang, J., Hong, F. J., and Cheng, P. Transient effects of mass convection in sessile droplet evaporation: the role of liquid and substrated thermophysical properties. *International Journal of Heat and Mass Transfer 117* (2017), 2072 – 2087.

[15] Cooke, J. R. Some theoretical considerations in stomatal diffusion: A field theory approach. *Acta Biotheoretica 17* (1967), 95–124.

[16] Dehaeck, S., Rednikov, A., and Colinet, P. Vapor-based interferometric measurement of local evaporation rate and interfacial temperature of evaporating droplets. *Langmuir 30*, 8 (03 2014), 2002–2008.

[17] Dollet, B., and Boulogne, F. Natural convection above circular disks of evaporating liquids. *Phys. Rev. Fluids 2* (May 2017), 053501.

[18] Dressaire, E., Yamada, L., Song, B., and Roper, M. Mushrooms use convectively created airflows to disperse their spores. *Proceedings of the National Academy of Sciences 113*, 11 (2016), 2833–2838.

[19] Dugas, V., Broutin, J., and Souteyrand, E. Droplet evaporation study applied to dna chip manufacturing. *Langmuir 21*, 20 (2005), 9130–9136. PMID: 16171342.

[20] Edwards, D., and Catton, I. Prediction of heat transfer by natural convection in closed cylinders heated from below. *International Journal of Heat and Mass Transfer 12*, 1 (1969), 23–30.

[21] Graniela, M. E., and Ramírez, C. A. Effect of a sweeping air stream and gas–phase aspect ratio of an isothermal stefan diffusion column on the experimental estimation of binary gas diffusivities. *Chemical Engineering Communications 206*, 7 (2019), 842–860.

[22] Hales, A. L. Convection currents in geysers. *Geophysical Supplements to the Monthly Notices of the Royal Astronomical Society 4* (1937), 122–131.

[23] Heinzelmann, F. J., Wasan, D. T., and Wilke, C. R. Concentration profiles in stefan diffusion tube. *Industrial & Engineering Chemistry Fundamentals 4*, 1 (1965), 55–61.

[24] Hsieh, S.-S., and Kuo, N.-H. Analysis of evaporation in the presence of composition/temperature gradient induced natural convection. *International Journal of Heat and Mass Transfer 36*, 4 (1993), 1097–1112.

[25] Kelly-Zion, P. L., Pursell, C. J., Booth, R. S., and VanTilburg, A. N. Evaporation rates of pure hydrocarbon liquids under the influences of natural convection and diffusion. *International Journal of Heat and Mass Transfer 52*, 13 (2009), 3305–3313.

[26] Kelly-Zion, P. L., Pursell, C. J., Wasson, G. N., Mandelkorn, B. V., and Nkinthorn, C. Correlation for sessile drop evaporation over a wide range of drop volatilities, ambient gases and pressures. *International Journal of Heat and Mass Transfer 118* (2018), 355 – 367.

[27] Kimura, S., and Bejan, A. The "heatline" visualization of convective heat transfer. *Journal of Heat Transfer 105*, 4 (1983), 916–919.

[28] Love, R. R. The electric field of two equal circular co-axial conducting disks. *The Quarterly Journal of Mechanics and Applied Mathematics 2*, 4 (01 1949), 428–451.

[29] Markham, B., and Rosenberger, F. Velocity and concentration distribution in a stefan diffusion tube. *Chemical Engineering Communications 5*, 5-6 (1980), 287–298.

[30] McBain, G. D., Suehrcke, H., and Harris, J. A. Evaporation from an open cylinder. *International Journal of Heat and Mass Transfer 43* (2000), 2117–2128.

[31] Medrado, J. P., Inman, R. H., and Coimbra, C. F. Pool evaporation under low grashof number downward convection. *International Journal of Heat and Mass Transfer 181* (2021), 122021.

[32] Medrado, J. P. T., Inman, R. H., and Coimbra, C. F. M. Non-isothermal free evaporation from open tubes. *International Journal of Heat and Mass Transfer* (Under review).

[33] Meyer, J., and Kostin, M. Circulation phenomena in stefan diffusion. *International Journal of Heat and Mass Transfer 18*, 11 (1975), 1293–1297.

[34] Mills, A. F., and Coimbra, C. F. M. *Mass Transfer*, 3rd ed. Temporal Publishing, San Diego, 2016.

[35] Nunez, G. A., and Sparrow, E. M. Models and solutions for isothermal and nonisothermal evaporation from a partially filled tube. *International Journal of Heat and Mass Transfer 31*, 3 (1988), 461–477.

[36] Ostroumov, G. A. Free convection under the conditions of the inertial problems. *NACA Tech. Memo. 1407* (1958).

[37] Pera, L., and Gebhart, B. Natural convection flows adjacent to horizontal surfaces resulting from the combined buoyancy effects of thermal and mass diffusion. *International Journal of Heat and Mass Transfer 15*, 2 (1972), 269 – 278.

[38] Ristenpart, W. D., Kim, P. G., Domingues, C., Wan, J., and Stone, H. A. Influence of substrate conductivity on circulation reversal in evaporating drops. *Phys. Rev. Lett. 99* (Dec 2007), 234502.

[39] Sharpley, B. F., and Boelter, L. M. K. Evaporation of water into quiet air from a one-foot diameter surface. *Industrial & Engineering Chemistry 30*, 10 (1938), 1125–1131.

[40] Shevchenko, V., Mialdun, A., Yasnou, V., Lyulin, Y., Ouerdane, H., and Shevtsova, V. Investigation of diffusive and optical properties of vapour-air mixtures: The benefits of interferometry. *Chemical Engineering Science 233* (2021), 116433.

[41] Shin, B., Ha, J., Lee, M., Park, K., Park, G. H., Choi, T. H., Cho, K.-J., and Kim, H.-Y. Hygrobot: A self-locomotive ratcheted actuator powered by environmental humidity. *Science Robotics 3*, 14 (2018).

[42] Sparrow, E. M., Kratz, G. K., and Schuerger, M. J. Evaporation of water from a horizontal surface by natural convection. *Journal of Heat Transfer 105*, 3 (08 1983), 469–475.

[43] Sparrow, E. M., and Nunez, G. A. Experiments on isothermal and non-isothermal evaporation from partially filled, open-topped vertical tubes. *International Journal of Heat and Mass Transfer 31*, 7 (1988), 1345–1355.

[44] Stewartson, K. On the free convection from a horizontal plate. *Zeitschrift für angewandte Mathematik und Physik ZAMP 9*, 3 (Sep 1958), 276–282.

[45] Sun, W., and Yang, F. Evaporation of a volatile liquid lens on the surface of an immiscible liquid. *Langmuir 32*, 24 (2016), 6058–6067.

[46] Tetens, O. Uber einige meteorologische begriffe. *Z. Geophys 6* (1930), 297–309.

[47] Verhoeven, J. D. Experimental study of thermal convection in a vertical cylinder of mercury heated from below. *The Physics of Fluids 12*, 9 (2021/03/01 1969), 1733–1740.

[48] Verwey, C., and Birouk, M. Experimental investigation of the effect of natural convection on the evaporation characteristics of small fuel droplets at moderately elevated temperature and pressure. *International Journal of Heat and Mass Transfer 118* (2018), 1046 – 1055.

[49] Vlasov, V. A. Diffusion-kinetic model of liquid evaporation from a stefan tube: A solution to the stefan diffusion problem. *International Journal of Heat and Mass Transfer 163* (2020), 120379.

[50] Vynnycky, M., and Maeno, N. Axisymmetric natural convection-driven evaporation of water: Analysis and numerical solution. *International Journal of Heat and Mass Transfer 55*, 21 (2012), 6238 – 6249.

[51] Xue, G., Xu, Y., Ding, T., Li, J., Yin, J., Fei, W., Cao, Y., Yu, J., Yuan, L., Gong, L., Chen, J., Deng, S., Zhou, J., and Guo, W. Water-evaporation-induced electricity with nanostructured carbon materials. *Nature Nanotechnology 12*, 4 (2017), 317–321.

[52] Yoon, S. G., Yang, Y., Yoo, J., Jin, H., Lee, W. H., Park, J., and Kim, Y. S. Natural evaporation-driven ionovoltaic electricity generation. *ACS Applied Electronic Materials 1*, 9 (09 2019), 1746–1751.

[53] Zhang, Z., Li, X., Yin, J., Xu, Y., Fei, W., Xue, M., Wang, Q., Zhou, J., and Guo, W. Emerging hydrovoltaic technology. *Nature Nanotechnology 13*, 12 (2018), 1109–1119.

[54] Zhao, Z., Hwang, Y., Yang, Y., Fan, T., Song, J., Suresh, S., and Cho, N.-J. Actuation and locomotion driven by moisture in paper made with natural pollen. *Proceedings of the National Academy of Sciences 117*, 16 (2020), 8711–8718.